Title

Organ geometry channels cell fate in the Arabidopsis ovule primordium

Elvira Hernandez-Lagana[1]*, Gabriella Mosca[2]*, Ethel Mendocilla Sato[2]*, Nuno Pires[2], Anja Frey[2,4], Alejandro Giraldo-Fonseca[2], Ueli Grossniklaus[2], Olivier Hamant[3], Christophe Godin[3], Arezki Boudaoud[3,5], Daniel Grimanelli[1], Daphné Autran[1#], Célia Baroux[2#]

1 Diversité, Adaptation et Développement des Plantes (DIADE), IRD, CIRAD, University of Montpellier, Montpellier, France.
2 Department of Plant and Microbial Biology and Zurich-Basel Plant Science Center, University of Zürich, Zürich, Switzerland.
3 Laboratoire Reproduction et Développement des Plantes, University of Lyon, ENS Lyon, UCB Lyon 1, CNRS, INRAE, INRIA, Lyon, France.
4 Present address: Novartis Pharma Schweiz AG, Basel, Switzerland.
5 Present address: LadHyX, Ecole polytechnique, CNRS, Institut Polytechnique de Paris, 91128 Palaiseau Cedex, France
* equal contribution.
# authors for correspondence: daphne.autran@ird.fr, cbaroux@botinst.uzh.ch

The authors declare no competing financial interests.

Running title

Organ shape and germinal fate in plant ovules.

ORCID numbers

Name	Orcid #
Elvira Hernandez-Lagana	0000-0002-2645-3783
Gabriella Mosca	0000-0003-4509-498X
Ethel Mendocilla Sato	0000-0003-0339-3535
Alejandro Giraldo-Fonseca	0000-0003-2943-9810
Nuno Pires	0000-0002-7113-3519
Anja Frey	
Ueli Grossniklaus	0000-0002-0522-8974
Olivier Hamant	0000-0001-6906-6620
Arezki Boudaoud	0000-0002-2780-4717
Christophe Godin	0000-0002-1202-8460
Daniel Grimanelli	0000-0001-5424-114X
Daphné Autran	0000-0002-5227-8966
Célia Baroux	0000-0001-6307-2229

Summary

In multicellular organisms, sexual reproduction requires the separation of the germline from the soma. In flowering plants, the first cells of the germline, so-called spore mother cells (SMCs), differentiate as the reproductive organs form. Here, we explored how organ growth influences and contributes to SMC differentiation. We generated a collection of 92 annotated 3D images capturing ovule primordium ontogeny at cellular resolution in Arabidopsis. We identified a spatio-temporal pattern of cell divisions that acts in a domain-specific manner as the primordium forms, which is coupled with the emergence of a single SMC. Using tissue growth models, we uncovered plausible morphogenetic principles involving a spatially confined growth signal, differential mechanical properties, and cell growth anisotropy. Our analysis also reveals that SMC characteristics first arise in more than one cell but SMC fate becomes progressively restricted to a single cell during organ growth. Altered primordium geometry coincided with a delay in this fate restriction process in *katanin* mutants. Altogether, our study suggests that tissue geometry canalizes and modulates reproductive cell fate in the Arabidopsis ovule primordium.

Keywords

ovule primordium, SMC, cell fate, plasticity, growth, tissue geometry, tissue mechanics, Arabidopsis

43 ## Introduction

44 A hallmark of sexual reproduction in multicellular organisms is the separation of the germline from the
45 soma. In animals, primordial germ cells (PGCs) are set-aside during embryogenesis from a mass of
46 pluripotent cells. The number of germ cells depends on the balance between proliferation (self-renewal)
47 and differentiation, a process controlled by both intrinsic factors signals from and the surrounding
48 somatic tissues. In flowering plants, the first cells representing the germline, the spore mother cells
49 (SMCs), differentiate only late in development. SMCs arise multiple times, in each flower during the
50 formation of the reproductive organs. In Arabidopsis, the female SMC differentiates in the nucellus of
51 the ovule primordium, a digit-shaped organ that emerges from the placental tissue of the gynoecium.
52 The SMC is recognizable as a single, large, and elongated subepidermal cell, in a central position, within
53 the nucellus, displaying a prominent nucleus and nucleolus (Bajon, 1999; Bowman, 1993; Schmidt et al.,
54 2015; Schneitz, 1995).

55 Although SMC singleness may appear to be robust, more than one SMC candidate *per* primordium is
56 occasionally seen, yet at different frequencies depending on the *Arabidopsis* accession (9,6% in
57 *Columbia* (*Col-0*), 27% in *Monterrosso* (*Mr-0)*, (Rodriguez-Leal et al., 2015). Mutants in *Arabidopsis*,
58 maize, and rice SMC singleness is compromised have unveiled the role of regulatory pathways involving
59 intercellular signaling, small RNAs, as well as DNA and histone methylation (Garcia-Aguilar et al., 2010;
60 Mendes et al., 2020; Nonomura et al., 2003; Olmedo-Monfil et al., 2010; Schmidt et al., 2011; Sheridan
61 et al., 1996; Sheridan et al., 1999; Su et al., 2020; Su et al., 2017; Zhao et al., 2008). As the SMC forms,
62 cell-cycle regulation contributes to the stabilization of its fate in a cell-autonomous manner through
63 cyclin-dependent kinase (CDK) inhibitors and RETINOBLASTOMA-RELATED1 (RBR1) (Cao et al., 2018;
64 Zhao et al., 2017). SMC singleness thus appears to result from a two-step control: first, by restricting
65 differentiation to one cell and second, by preventing self-renewal before meiosis (reviewed in (Lora et
66 al., 2019; Pinto et al., 2019).

67 However, the precise mechanisms underlying the plasticity in the number of SMC candidates and SMC
68 specification are still poorly understood. In principle, SMC singleness may be controlled by successive
69 molecular cues. However, even in that scenario, such cues must be positional, at least to some extent,
70 and thus involve a spatial component. Over the last decade, many different molecular cues defining
71 spatial patterns in the ovule primordium were identified (Pinto et al., 2019; Su et al., 2020), however
72 their coordination is unknown. Since SMCs emerge at the primordium apex concomitant with its

elongation, we hypothesize that geometric constraints during ovule morphogenesis influence SMC singleness and differentiation. Such an hypothesis could explain variation in the number of SMC candidates, ultimately culminating in a single SMC entering meiosis. Answering the questions of whether SMC formation follows a stereotypical or plastic developmental process and whether it is intrinsically linked to or independent of ovule primordium formation would unravel fundamental principles connecting cell fate establishment and organ growth.

Such an analysis requires a high-resolution description of ovule geometry during development. Our current knowledge of ovule primordium growth in *Arabidopsis* is based on two-dimensional (2D) micrographs from tissue sections or clearings. It is described in discrete developmental stages capturing classes of primordia by their global shape and SMC appearance until meiosis and by the presence of integument layers and ovule curvature later-on (Grossniklaus et al., 1998). In addition, a 3D analysis of average cell volumes during primordium growth was recently provided (Lora et al., 2017). Yet, we lack a view of the patterning processes regulating early ovule primordium formation and how the dynamics of cell proliferation contributes to the cellular organization during primordium growth. We thus described and quantified the growth of the ovule primordium at cellular resolution in 3D. We combined 3D imaging, quantitative analysis of cell and tissue characteristics, reporter gene analyses, 2D mechanical growth simulations. In addition, using the *katanin* mutant that affects anisotropic cell growth and cell division patterns (Luptovciak, Komis, et al., 2017; Ovecka et al., 2020), we show that altered ovule morphology lead to ectopic SMC candidates. We also uncovered that differentiation of SMC candidates initiate earlier than previously thought, and provide evidence for a gradual process of cell fate restriction, channeling the specification of a single SMC prior to meiosis.

Results

Building a reference image dataset capturing ovule primordium development at cellular resolution

To generate a reference image dataset describing ovule primordium development in 3D and with cellular resolution, we imaged primordia at consecutive stages in intact carpels by confocal microscopy. Carpels were cleared and stained for cell boundaries using a modified PS-PI staining (Truernit et al., 2008) and mounted using a procedure preserving their 3D integrity (Mendocilla-Sato, 2017) (Figure 1A). We selected high signal-to-noise ratio images and segmented them based on cell boundary signals using Imaris (Bitplane, Switzerland) as described previously (Mendocilla-Sato, 2017) (Figure 1B). We manually curated 92 ovules representing seven consecutive developmental stages (7-21 ovules *per* stage, Figure 1B, Table 1, Source Data 1), classified them according to an extended nomenclature (explained in Materials and Methods). The temporal resolution of our analysis led us to subdivide early stages (stage 0-I to stage 0-III) covering primordium emergence prior to the straight digit-shape of the organ set as stage 1-I, where the SMC becomes distinguishable by its apparent larger size in longitudinal views (Grossniklaus et al., 1998) (Figure 1B).

To evaluate the distinct contribution of domain-, layer- and cell-specific growth dynamics, we labeled cells depending on their belonging to different regions of the ovule primordium: apical vs basal domains, L1/L2/L3 layers. In addition we associated each cell with a cell type: “L1 apical”, “L1 basal”, “L2,L3 apical”, “L2,L3 basal”, “SMC”, “L1 dome” (for the upmost apical L1 cells in contact with the SMC), “CC” (for companion cells, elongated L2 cells adjacent to the SMC) (Figure 1B, Materials and Methods).

To generate a quantitative description of ovule primordia with respect to cell number, size and shape according to cell labels, layers, domains, ovule stage and genotype, we developed an interactive, R-based interface named OvuleViz. The interface imports cell descriptors exported from segmented image files and enables multiple plots from a user-based selection of (sub)datasets (Figure supplement 1A-C, Materials and Methods). This work generated a reference collection of annotated, 3D images capturing ovule primordium development at cellular resolution from emergence until the onset of meiosis. The collection of 92 segmented images comprising a total of 7763 annotated cells and five morphological cell descriptors (volume, area, sphericity, prolate and oblate ellipticity) provides a unique resource for morphodynamic analyses of ovule primordium growth.

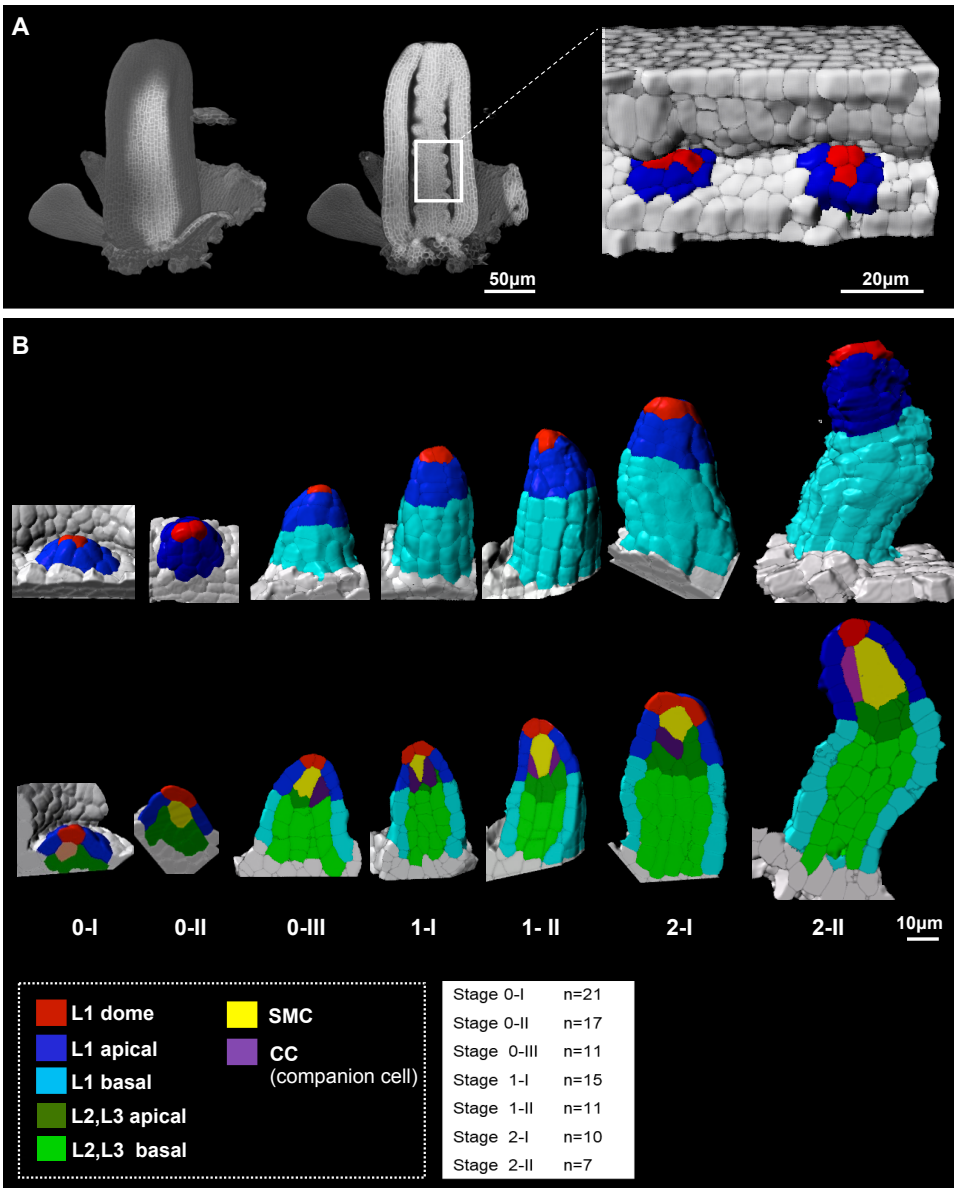

Figure 1. Reference set of 3D segmented images capturing Arabidopsis ovule primordium growth at cellular-resolution.

(A) 3D reconstruction of a whole gynoecium stained with PS-PI (cell wall dye) and visualized by CSLM. The cross section allows showing the nascent ovule primordia attached to the placenta.

(B) Ovule primordium developmental stages (0-I to 2-II) and organ viewpoints (domains) defined for the 3D quantitative analysis. All segmented data can be analyzed by an interactive interface named OvuleViz. See also Figure supplement 1A-C.

n= number of ovules analyzed. Segmented images for all developmental stages are provided in Source Data 1. See also Figure supplement 1 D-E, Materials and Methods.

141

	0-I			0-II			0-III		
Cells above placenta*	2.5	(±3.5)	(n=21)	3.6	(±0.5)	(n=17)	5.9	(±1.0)	(n=11)
range (min-max)	2	-	3	3	-	4	5	-	8
total # cells	28	(±5.7)	(n=21)	38	(±8.0)	(n=17)	80	(±8.4)	(n=11)
width (µm) (W)	23	(±3.5)		26.3	(±2.4)		28.0	(±3.1)	
height (µm) (H)	5.3	(±1.2)		11.9	(±2.1)		22.5	(±3.6)	
H:W ratio	0.2	(±0.04)	(n=13)	0.45	(±0.06)	(n=14)	0.8	(±0.12)	(n=8)

	1-I			1-II		
cells above placenta*	7.3	(±1.3)	(n=15)	9.7	(±1.0)	(n=11)
range (min-max)	6	-	10	8	-	11
total # cells	105	(±10.6)	(n=15)	128	(±18.0)	(n=11)
width (µm) (W)	27	(±2.0)		27.8	(±3.5)	
height (µm) (H)	30	(±2.8)		39	(±5.9)	
H:W ratio	1.1	(±0.10)	(n=6)	1.4	(±0.22)	(n=8)

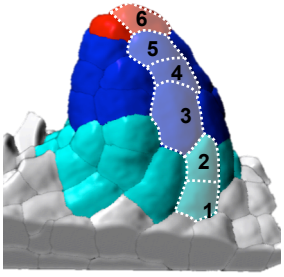

	2-I			2-II		
cells above placenta*	10	(±1.1)	(n=10)	12.6	(±1.0)	(n=7)
range (min-max)	9	-	12	11	-	14
total # cells	151	(±18.9)	(n=10)	165	(±19.8)	(n=7)

* scoring the length of L1 cell file above placenta

142 **Table 1. Classification criteria of Arabidopsis ovule primordia.**

143 The table summarizes general characteristics of ovule primordia per stage: cell "layers" above the placenta scored
144 as the number of L1 cells in a cell file drawn from the basis to the top, range thereof, total cell number, ovule
145 shape including height, width, aspect ratio. See also Source Data 1.

146
147
148 To identify correlations between growth patterns and differentiation, we first performed a
149 principle component analysis (PCA) based on the aforementioned cell descriptors, *per* cell type and
150 stage, considered together or separately (Figure supplement 1D-E). In this global analysis, the SMC
151 appears morphologically distinct at late stages (2-I and 2-II) but not at early stages. This prompted us to
152 investigate in detail the contribution of different layers, domains, and cell types to ovule primordium
153 growth and in relation to SMC differentiation.

154

155 **Ovule primordium morphogenesis involves domain-specific cell proliferation and anisotropic cell**
156 **shape patterns**
157
158 The ovule primordium emerges from the placenta as a small dome-shaped protrusion and grows
159 into a digit-shaped primordium with nearly cylindrical symmetry (stage 1-I) before enlarging at the base
160 (Figure 1B). Using our segmented images, we first quantified global changes in cell number, cell volume,
161 and ovule primordium shape. Our analysis revealed two distinct phases of morphological events. Phase I
162 (stages 0-I to 0-III) is characterized by a 4.5-fold increase in total cell number together with a moderate
163 increase in mean cell volume (10%, P=0.03). By contrast, Phase II (stages 1-I to 2-II) is characterized by a
164 moderate increase in cell number (50%) and the global mean cell volume is relatively constant (Figure
165 2A, Figure supplement 2A). To quantify the resulting changes in organ shape, we extrapolated a
166 continuous surface mesh of the ovule outline and used it to compute its height and width at the base
167 (Figure 2B-C, Figure supplement 2B, Supplemental File 1). Anisotropic organ growth during Phase I was
168 confirmed by a steady increase in height while primordium width increased moderately (Figure 2C). This
169 contrast in events between Phase I and II is illustrated by the fold-changes (FCs) in cell number and
170 aspect ratio (Figure 2D) which range between 1.5 and 2.0 in Phase I whereas drop to 1.4 and 1.2 in
171 Phase II, respectively. These observations confirmed that Phase I captures a distinct growth dynamic
172 compared to Phase II.
173 Next, to capture possible specific patterns of growth, we analyzed cell number, cell size, and cell
174 shape using different viewpoints: one comparing the L1 and L2-L3 layers and one contrasting the apical
175 *vs.* basal domains. Counting cell number *per* viewpoint clearly showed a dominant contribution of the
176 epidermis (L1) relative to the subepidermal layers and of the basal relative to the apical domain (Figure
177 2E, 2F). To verify these findings with a cellular marker, we analyzed the M-phase-specific
178 *promCYCB1.1::CYCB1.1-db-GFP* reporter (abbreviated CYCB1.1db-GFP) (Ubeda-Tomas et al., 2009). We
179 scored the number of GFP-expressing cells among 481 ovules and plotted relative mitotic frequencies
180 *per* cell layer and domain for each ovule stage to generate a cell-based mitotic activity map (Figure 2G-
181 H, Source Data 2, Materials and Methods). In this approach, subepidermal (L2) cells beneath the dome
182 were distinguished from underlying L3 cells to gain resolution on the L2 apical domain where the SMC
183 differentiate. Consistent with our previous observation, in Phase I, a high proliferation activity was
184 scored in L1 cells at the primordium apex (scoring 64% of mitotic events). By contrast, the L2 apical
185 domain remains relatively quiescent (contributing only 3% of the mitotic events). During Phase II, the
186 majority (60%) of mitotic events is found in the basal domain, consistent with the progressive
187 population of the basal domain. It is noteworthy that during this phase, few mitotic events are detected

in L2 apical cells, with the exception of SMC neighbor cells that show frequent divisions at stage 1-II. Thus, genetic reporter analysis confirmed a biphasic, temporal pattern of cell division with changing regional contributions, suggesting the L1 dome and the basal domain as consecutive sites of proliferation, contributing to morphological changes in Phase I and II, respectively.

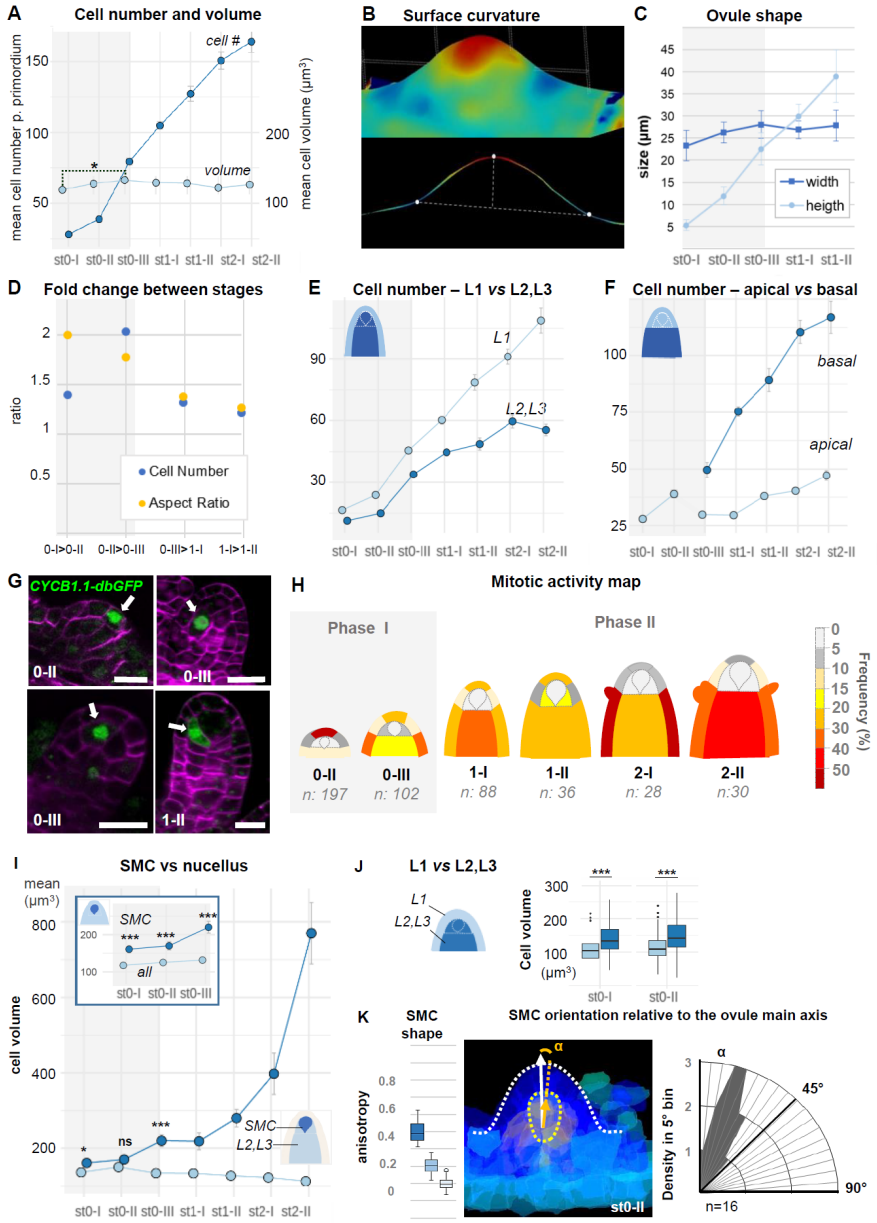

Figure 2. Ovule primordium morphogenesis involves domain-specific cell division and anisotropic cell growth.
(A) Mean cell number *per* ovule increases mainly during stages 0-I to 0-III (Phase I), whereas cell volume *per* ovule remains constant on average across primordium development (stages 0-I to 2-II).
(B) Representative image of a continuous surface of an ovule primordium mesh and its projected median plane. Dashed lines indicate the minimal and maximal curvature points used to measure organ height and width. Color scale: minimal curvature mm-1 (see also Figure supplement 2B).

199 **Figure 2. Ovule primordium morphogenesis involves domain-specific cell division and anisotropic cell growth**
200 **(*continued*).**
201 (C) Anisotropic organ growth during Phase I and until stage 1-II. Mean width and height were quantified *per* stage.
202 (D) Phase I captures a distinct growth dynamic compared to Phase II. Fold-change of cell number and aspect ratio
203 between stages are plotted.
204 (E) Mean cell number is increased at the L1 *versus* L2,L3 layers across developmental stages.
205 (F) Mean cell number is increased in the basal *versus* apical domain across developmental stages.
206 (G) Representative images of ovule primordia expressing the M-phase reporter *promCYCB1.1::CYCB1.1db-GFP*
207 (CYCB1.1db-GFP). White arrows indicate dividing cells. Magenta signal: Renaissance SR2200 cell-wall label. Scale
208 bar: 10µm.
209 (H) Domain-specific map of mitotic activity during ovule primordium development, scored using the CYCB1.1db-
210 GFP reporter. The frequency of mitoses was calculated *per* ovule domain at each developmental stage and color-
211 coded as indicated in the bar (right). n: total number of scored ovules.
212 (I) Mean SMC candidate volume (dark blue) is significantly increased as compared to L2,L3 cells (pale blue) from
213 stage 0-III onward, on even at earlier stages as compared to all other cells (inset).
214 (J) Mean cell volume is increased in L2,L3 cells as compared to L1 cells, at the two early developmental stages (0-I,
215 0-II).
216 (K) The SMC consistently displays anisotropic shape with main axis of elongation aligned with ovule growth axis.
217 The SMC anisotropy index (boxplot, left; stage 0-II, n=16 ovules) was calculated from the Maximum (dark blue),
218 Minimum (light blue) and Medium (medium blue) covariance matrix eigenvalues, computed from 3D segmented
219 cells (see Figure supplement 2G). Image (middle): illustration of the SMC main anisotropy axis (orange arrow)
220 related by an angle 'alpha' to the main axis of the ovule primordium (white arrow), stage 0-II. Radar plot (right):
221 'alpha' angle measured on z projections for n=16 ovule primordia at stage 0-II. See also Materials and Methods.
222 Error bars: Standard errors to the mean. Differences between cell types or primordium domains were assessed
223 using a two-tailed Man Whitney U test in (A) and (I); a two-tailed Wilcoxon signed rank test in (J). *p≤0.05,
224 **p≤0.01, ***p≤0.001. See also Figure supplement 2, Source Data 2, Materials and Methods.

225

226 Average cell size analysis, by contrast, did not reveal significant changes during primordium
227 development with the notable exception of the SMC (Figure 2A, Figure supplement 2C). The distinct size
228 of the SMC candidate is already detected at stage 0-III when compared to other L2,L3 cells (Figure 2I) or
229 even earlier (stage 0-I), when compared to all other cells (Figure 2I inset). Size differentiation of the SMC
230 is not uniform among ovules, demonstrating plasticity in the process (Figure supplement 2D). In
231 addition, cells from the L2 and L3 layers are larger than L1 cells already at stage 0-I (Figure 2J, Figure
232 supplement 2E) possibly due to a longer growth phase, consistent with the low division frequency
233 observed previously.

234 We then investigated cell shape changes during primordium elongation, using ellipticity and
235 sphericity indices computed following segmentation. The analysis did not reveal significant differences
236 between domains or layers (Figure supplement 2F). This could indicate either a highly variable cell shape
237 or local, cell-specific differences. We thus more specifically analyzed the subepidermal domain where
238 the SMC differentiates. Companion cells showed an increasing ellipticity (and decreasing sphericity),

239 starting at stage 1-I and culminating at stage 2-I (Figure supplement 2F). By contrast, the SMC only
240 showed a moderate decrease in sphericity at late stages and no distinctive ellipticity at early stages
241 (Figure supplement 2F) when compared to other cells. To get more information on SMC shape, we
242 compared the maximum, medium and minimum anisotropy index. For this, we developed an extension
243 for MorphoMechanX (Barbier de Reuille et al., 2015), (www.morphomechanx.org) to (i) perform a semi-
244 automatic labeling of cell layers and cell types from a cellularized mesh obtained from segmentation
245 data and (ii) compute in each 3D cell the principal axes of shape anisotropy and the corresponding
246 indexes (Figure supplement 2G, Supplemental File 1, movie in Supplemental File 2). The averaged
247 maximum anisotropy shape index of the SMCs was consistently above the medium (and hence above
248 the minimum) anisotropy index (Figure 2K, Figure supplement 2H). We measured the degree of
249 alignment of the SMC major axis with the main growth axis of the ovule during early stages (stage 0-II)
250 and found a mean angle of 22° (+/- 11°, n=16) (Figure 2K). This confirmed that the SMC has a consistent
251 anisotropic shape from early stage onwards, with a distinguishable major axis aligned with primordium
252 axis.

253 Taken together, these results suggest that anisotropic primordium growth is linked to a biphasic,
254 domain-specific cell proliferation, alternating between the L1 dome at phase I and the basal domain at
255 phase II, combined with localized, anisotropic expansion in the L2 apical domain. In this process, SMC
256 characteristic distinct size, anisotropic shape and orientation aligned with the growth axis of the
257 primordium emerge already in Phase I, while entering a pronounced growth and elongation at Phase II
258 concomitantly to organ shape elongation. While primordium elongation is not explained by anisotropic
259 cell growth alone but also by cell proliferation (Figure supplement 2F), the observation that cells are
260 elliptic suggests a potential role for anisotropic cell growth. We explore this property in the next section
261 through an *in-silico* approach.

262

263 2D mechanical simulations of ovule primordium development relate its coordinated growth to SMC 264 shape emergence

265 Organ shape is determined by the rate and direction of cell growth, in turn affected by signaling
266 and the mechanical state of the tissue and its geometry, with possible feedback interactions between
267 them (Bassel et al., 2014; Echevin et al., 2019). Mechanical constraints arise from the growth process in
268 form of tensile and compressive forces that, in turn, influence cell and tissue growth depending on their
269 elastic/visco-plastic properties (Echevin et al., 2019). To determine the role of ovule primordium growth
270 on SMC differentiation, which involves early differential cell growth, we sought to understand the

contributions of local growth rate and anisotropy, and their relation to signaling and mechanical constraints (Coen et al., 2004; Kennaway et al., 2011).

We first aim at determining morphogenetic principles of primordium growth at the tissue level by developing a 2D Finite Element Method (FEM)-based mechanical model, which considered two uncoupled but complementary modes of growth (Bassel et al., 2014): (i) signal-based growth in which an abstract growth factor captures the cumulative effects of biochemical signals, without considering its explicit mode of action (i.e., cell wall loosening, increase in turgor pressure) (Boudon et al., 2015; Coen et al., 2004); and (ii) passive strain-based growth in which relaxation accommodates excess of strain (and therefore also excess of stress) that accumulated in the tissue, by relaxing its reference configuration according to the amount of strain(Boudon et al., 2015; Bozorg et al., 2016). The mechanical equilibrium is computed to ensure compatibility within the tissue that is locally growing at different rates and orientations. This introduces residual internal compressions and tensions to which the action of turgor pressure has to be added up (Boudon et al., 2015; Rodriguez et al., 1994). A polarization field is used to set the direction of anisotropic growth for both growth mechanisms (Coen et al., 2004). The simulation consists of iterations where the mechanical equilibrium is computed before each growth step is specified by signal- and strain-based growth (Supplemental File 1). This strategy extends previous tissue growth models (Bassel et al., 2014; Boudon et al., 2015; Bozorg et al., 2016; Kuchen et al., 2012; Mosca, 2018).

We designed a starting template consisting of an L1 layer distinct from the underlying L2, L3 tissue based on different growth and material properties (Table 2, Figure supplement 3, Supplemental File 1). We first set the model components to produce a realistic elongated, digit-shaped primordium with a narrow dome and an L1 layer of stable thickness during development, fitting experimental observation (Figure supplement 2C) (Reference Model, FEM-Model 1) (Figure 3A, Figure supplement 3A). This model combines the following hypotheses: an initial, narrow domain of anisotropic, signal-based growth with a high concentration in inner layers, a broad domain competent for passive strain-based relaxation and material anisotropy.

Modeling hypotheses		Models							
		1	2	3	4	5	6	7	8
Growth anisotropy		●	●	-	●	●	●	●	●
Material anisotropy		●	-	○	○	○	○	○	○
Passive Strain-based relaxation		●	●	●	●	●	●	●	-
Signal-based growth									
Distribution	L1 only	-	-	-	-	-	●	-	-
	Inner tissue only (pi-shape)	-	-	-	-	-	-	●	-
	L1 + inner tissue (pit-shape)	●	●	●	-	●	-	-	●
	L1 + inner tissue (broad distribution)	-	-	-	●	-	-	-	-
Fixed high concentration	L1 only	-	-	-	-	●	●	-	-
	Inner tissue only	-	-	-	-	-	-	●	-
	L1 + inner tissue	●	●	●	●	-	-	-	●

Table 2. Hypotheses used to generate the mass-spring (MS) and continuous Finite Element Method (FEM) based simulations.

Several growth and mechanical hypotheses were listed at start of modelling. To evaluate their effect on primordium growth each hypothesis was excluded (-) in at least one scenario. The FEM and mass-spring (MS) models presented in Figure 3 and S3 are numbered according to the scenarios (1-8) in the table. Since it is not possible for MS to simulate material anisotropy, Model 1 was only tested with FEM. The hypothesis of Growth anisotropy is always active for the L1 layer in the models reported in the table. Empty dots for "Material anisotropy" were considered only for the FEM models. See also Figure supplement 3 and Supplemental File 1 for modelling principles, results and detailed computational methods.

Then, using the versatility of the modeling framework to vary initial conditions, we tested the influence of the spatial distribution of the specified growth signal on primordium growth. As first variation, we let the growth signal diffuse broadly in the domain while maintaining the selected initial cells with prescribed high intensity growth signal (FEM-Model 4). The emerging primordium is appreciably broader than the Reference Model (Figure supplement 3B). We then explored what is the contribution of growth signal in the L1 compared to in inner tissue to the primordium growth. In model FEM-Model 5, prescribed high growth signal is present only in the L1 and it is free to diffuse in the inner layers. This model produced a sharp primordium, narrower and taller than the Reference Model, but does not preserve L1 thickness (Figure supplement 3B). The L2 apical domain is narrower as compared to the Reference Model. When the growth signal is absent in the inner tissue (FEM-Model 6), signal growth in the L1 alone is not sufficient to enable primordium growth (Figure supplement 3B).

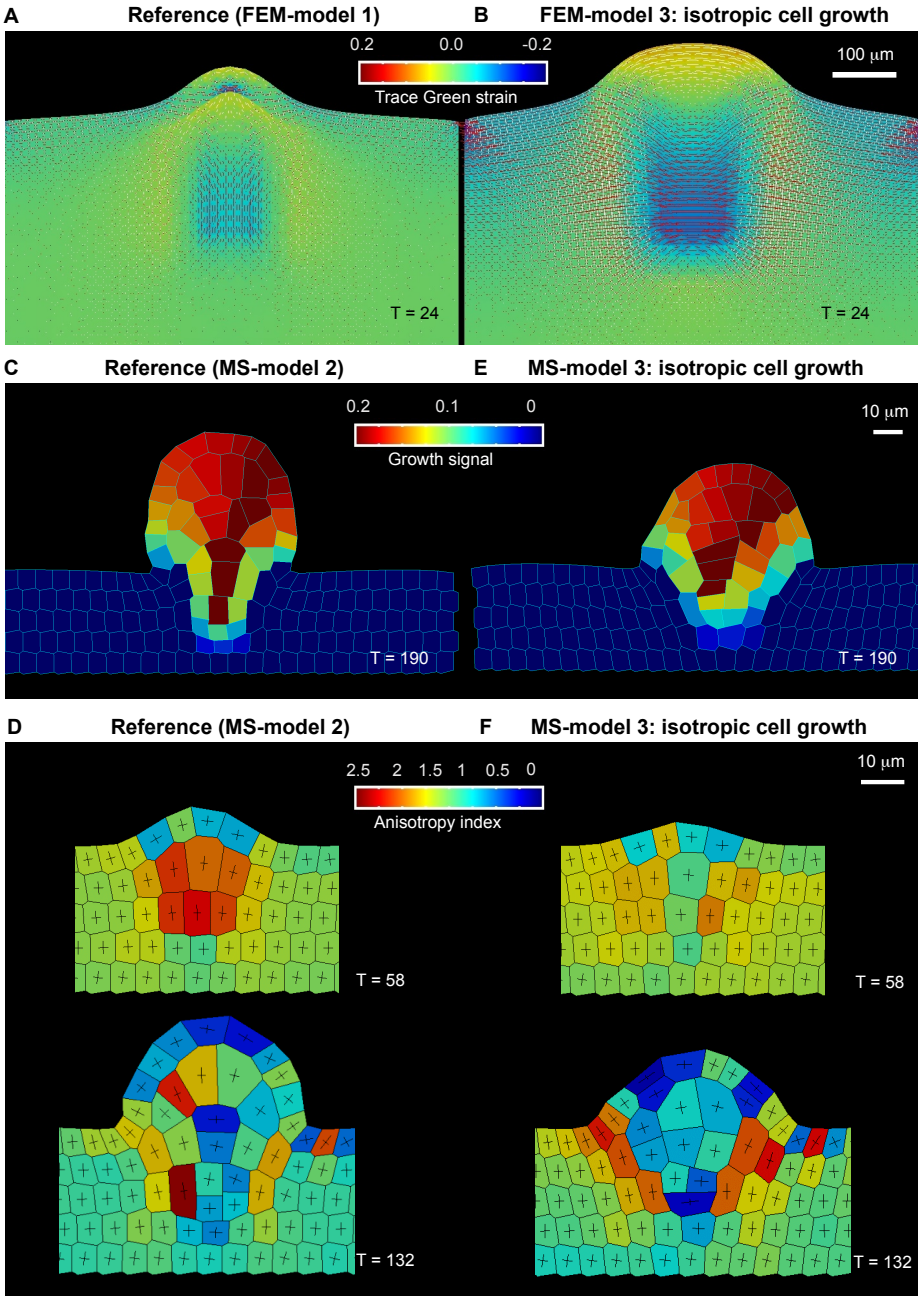

Figure 3. Mechanical and cell-based 2D simulation models of ovule primordium development predict that ovule shape depends on cell growth anisotropy.

(A-B) Finite Element Model (FEM), tissue-based simulations of ovule primordium growth. (A) Growth stability is reached at T=24 in the reference model FEM model 1. (B) Simulations omitting the anisotropic growth parameter (FEM-model 3) show abnormal ovule dome shape at the same simulation time. The level (Trace green strain) and principal directions (fine lines, white: expansive, red: compressive) of accumulated strain is shown.
(C-F) Mass Spring (MS) cell-based simulations of ovule primordium growth showing the growth signal distribution and anisotropy index at the indicated simulation times (T). (C) Reference model (MS-model 2) showing a realistic primordium shape with straight flanks, sharp curvature at the apex and narrow base at T=190. (D) The reference model shows the emergence of a large, anisotropic cell with trapezoidal shape in L2 at T=58, confirmed at T=132.

329 **Figure 3. Mechanical and cell-based 2D simulation models of ovule primordium development predict that ovule**
330 **shape depends on cell growth anisotropy (*continued*).**

331 (E) Simulation with isotropic cell growth in inner layers (MS-model 3) produces a primordium with enlarged apex
332 and basis and flatter dome at the same simulation time as in the reference model. (F) L2 cells in MS-model 3 show
333 reduced anisotropy as compared to the Reference model. See also Figure supplement 3, Table 2, Supplemental
334 File1 for modelling hypotheses and methods.
335

336 To answer the complementary question whether growth signal is required in the L1 to grow a
337 primordium when this is present in the inner layers, this hypothesis (Table 2) was removed in FEM-
338 Model 7 (Figure supplement 3B). This scenario indeed enables to grow a digit shape structure (as long as
339 strain-based growth is permitted), yet the dome appears shallower than the Reference Model.
340 To conclude, both models where high growth signal is selectively present only in L1 or in inner tissue
341 layers can produce a primordium. Yet, absence of growth signal in the inner layers result in drastic shape
342 alterations. This favors a scenario where inner tissue -driven growth has a fundamental role.

343 Next, through modulation of passive strain-based growth, we determined that a broad tissue
344 domain uniformly competent for strain accommodation is necessary to resolve the high accumulation of
345 stress, which limits primordium elongation (FEM-Model 8, Figure supplement 3C). We also explored the
346 contribution of material anisotropy (FEM-Model 2 and FEM-Model 2a, Figure supplement 3C): even in
347 the case of isotropic material, it is possible to grow a digit-shape protrusion, yet with a wider dome, and
348 an increased L1 thickness, in contrast with experimental observations. To restore the L1 thickness, it is
349 sufficient to prescribe material anisotropy in the L1 exclusively.
350 Finally, we asked whether growth anisotropy must be specified in the model or if organ geometry and
351 mechanical constraints are sufficient to specify primordium shape. Clearly, removing growth anisotropy
352 component abolished the digit shape of the primordium and produced a hemi-spherical protrusion
353 (FEM-Model 3, Figure 3B).
354

355 In summary, we identified parsimonious growth principles shaping the ovule primordium and
356 suggesting different contributions of the epidermis and inner layers: an active tissue growth, mostly
357 inner-driven and requiring a narrow, pit-shape domain of growth-signal, complemented by passive
358 tissue growth with a necessary response of the L1 to accommodate accumulated strain. Furthermore,
359 material anisotropy in the L1 is predicted to play a role in constraining L1 thickness as observed
360 experimentally.
361

362 Next, we aimed to analyze how cell division and cell shape, particularly that of the SMC, are
363 connected to tissue growth patterns at cellular scale. For this, we developed a complementary model
364 with cellular resolution. This vertex-based model features cells as 2D polygons whose walls are mass
365 spring (MS) segments (Amar, 2011; Smith, 2009). This model integrates mechanics (Hooke's law for MSs)
366 with signal- and strain-based growth as before (Supplemental File 1), and cells are able to divide after
367 they reach a threshold area, the newly inserted walls following the rule "shortest wall through centroid"
368 (Supplemental File 1). We simulated growth starting with a virtual grid of cells representing a flat
369 placenta and focused on early stages of ovule primordium formation until stage 1-I. We tested the same
370 combination of growth hypotheses as for the continuous model (Table 2), except for material anisotropy
371 that cannot be easily embedded in a vertex-based model. As we observed that L1 cells do not divide
372 periclinally, nor change in volume on average (see Figure supplement 2C), we deduced that their growth
373 occurs mainly along the surface of the primordium. For this reason, we enforced this feature in our
374 model, preventing growth of anticlinal walls in the L1 (both for signal-based growth and passive strain-
375 based growth, Supplemental file 1). This constraint limits the ways an organ can grow in a digit-shaped
376 fashion, as the L1 does not progressively populate the inner tissues by division. Furthermore, our models
377 allowed for larger cells in subepidermal layers compared to the epidermis, in agreement with our
378 observation (Figure supplement 2E).
379 We observed that MS-Model 2 best captures the characteristic shape and aspect ratio of ovules
380 (Figure 3C-D, Figure supplement 3D). This Reference Model confirmed the growth hypotheses from
381 FEM-based simulations regarding the distribution and orientation of signal-based growth (Figure
382 supplement 3B) and passive strain-based growth (Figure supplement 3C). Altering growth hypotheses
383 similarly to that in the FEM models produce similar results (Figure Supplement 3B,C), yet with more
384 dramatic shape changes in the case of lack of strain-based relaxation (MS-Model 8 and MS-Model 8a)
385 and growth signal concentration in inner tissue (MS-Model 5, Supplemental File 3). In the Reference
386 Model (MS-Model 2), an L2 apical cell with a trapezoidal shape, elongated along the main direction of
387 ovule growth, emerged consistently during simulation (note that these cells still divide in the models as
388 no special rule has been assigned to them) (Figure 3D). These are similar to SMC candidates at stage 0-II
389 in real primordia, in a 2D longitudinal, median section through the ovule (Figure 2K). The elongated-
390 trapezoidal shape of such cell is not a prescribed feature of the model, but rather emerges from the
391 combination of assigned anisotropic cell growth and geometrical constraints imposed by the
392 surrounding growing tissues.
393

394 Next, we wanted to explore the role of cell growth anisotropy in ovule primordium shape and
395 SMC emergence. The MS-Model 3 (Figure 3E-F) corresponds to a virtual mutant where cell growth was
396 set to isotropic in inner layers (the L1 was maintained with anisotropic growth to preserve its thickness).
397 This led to an ovule primordium with a wider and flatter dome, comparable to the FEM-Model 3.
398 Despite the absence of specified growth direction in inner tissue, due to geometrical constraints, the
399 primordium still grows mostly vertically. We wanted to assess whether such geometrical constraints
400 would enable the formation of an elongated, trapezoidal SMC candidate also in the case of prescribed
401 isotropic growth. As Figure 3E-F shows, the SMC candidate does not display a stereotypical shape and is
402 not even elongated. Yet, mild cell anisotropy can be reached if the SMC candidate is allowed to grow
403 twice more than in the reference model (Figure Supplement 3E, MS-Model 3a).
404 Altogether, the different simulations suggest that SMC anisotropy and characteristic shape can
405 also be an emerging property of ovule primordium growth connected to geometrical constraints, even
406 if, in the absence of specified anisotropic growth. The complementary model altering cell growth
407 anisotropy specifically in the L1 further suggested that directional cell growth in this layer is necessary to
408 accommodate inner-driven growth and permit primordium elongation (MS-Model 3b, Figure
409 supplement 3F).
410 In all of the above simulations, the candidate SMC eventually divided as the models missed a
411 causative rule to differentially regulate cell division. When we prevented the SMC candidate to divide,
412 its enlargement overrode primordium shape control in our simulations creating an enlarged dome
413 (Figure supplement 3G). This suggests that a mechanism may limit SMC growth in real primordia.
414 Altogether, 2D mechanical-based simulations in both continuous tissue, or cell-based
415 approaches confirmed a role for localized cell growth compatible with experimental observations. The
416 simulations also pointed to the importance of a differential role for the epidermis (accommodation) and
417 the inner tissue (major growth component) as well as anisotropic cell growth as necessary for ovule
418 primordium shape. Further, the simulations suggested that SMC formation can be an emerging property
419 of primordium geometry.
420

421 ### *katanin* mutants show a distinct ovule primordium geometry

422
423 To experimentally test the prediction of the isotropic growth models we analyzed ovule
424 primordium growth and SMC fate establishment in *katanin* mutants with well described and understood
425 geometric defects: in absence of the microtubule-severing protein KATANIN, the self-organization of
426 cortical microtubules in parallel arrays is hindered, thereby decreasing the cellulose-dependent

427 mechanical anisotropy of the wall and resulting in more isotropic growth (Bichet et al., 2001; Burk et al.,
428 2002). Here, we specifically analyzed the shape and cellular organization of ovule primordia in *katanin*
429 mutants using the *botero* (*bot1-7*) (*Ws* background), *lue1*, and *mad5* alleles (*Col* background) (Bichet et
430 al., 2001; Bouquin et al., 2003; Brodersen et al., 2008), collectively referred to *katanin* - noted *kat* -
431 mutants hereafter. We generated and analyzed a new dataset of 59 annotated 3D digital *kat* and
432 corresponding wild-type ovule primordia at stages 0-III, 1-I, and 1-II (Source Data 4A). *kat* mutant
433 primordia clearly showed an increased size and a more isotropic shape (Figure 4A), being 1.5 times
434 bigger in volume than wild-type primordia (P=0.007, stage 0-III, Figure 4B) with a smaller aspect ratio
435 (P<0.01 stages 1-I, 1-II, Figure 4C). Because the width-to-height ratio does not inform on the shape at
436 the flanks, we derived an equation to estimate the "plumpiness" of the primordia: primordia with
437 rounder flanks will have a higher bounding box occupancy, that is, the volume fraction of a fitting, 3D
438 parallelepiped (bounding box) effectively occupied by the primordium (Figure 4D, left), than straight-
439 digit shape ovules of the same aspect ratio. Mutant primordia clearly deviate from wild-type primordia
440 in their relationship between aspect ratio and bounding box occupancy relationship at stage 1-I (Figure
441 4D, Figure supplement 4A), when the primordium normally starts elongating along the major growth
442 axis. These measurements confirmed a marked attenuation of anisotropic growth in *kat* ovule primordia
443 as was observed in roots, shoot organs, or seeds (Bichet et al., 2001; Hervieux et al., 2016; Luptovciak,
444 Samakovli, et al., 2017; Ren et al., 2017; Uyttewaal et al., 2012; Wightman et al., 2013; Zhang et al.,
445 2013). Yet, at a global level, the mean cell number, cell volume, and sphericity are not significantly
446 different between *kat* and wild-type primordia (Figure supplement 4B-C). Thus, these global approaches
447 did not resolve the origin of primordia mis-shaping.

448 To refine the analysis, we contrasted different layers as done for wild-type primordia and found
449 local alterations that provide an explanation for the formation of broader and more isotropic primordia
450 in *kat* mutants. Indeed, at stage 0-III *kat* ovules display a broader epidermis domain composed of more
451 and larger cells than in wild-type (P=0.03 and P<0.001, respectively) (Figure 4E). Mitosis frequency
452 analysis indicated a shift in cell division from the apex towards the basis (2.4 times less mitoses in the L1
453 dome domain and 2.7 times more in the L1 basal domain, compared to wild-type) (Figure 4F, Figure
454 supplement 4E), consistent with the increased cell number observed in L1. Yet increased divisions is not
455 a general characteristic of *kat* primordia since overall, the apical and basal domains are not massively
456 overpopulated. By contrast, *kat* cells are generally larger and slightly more spherical in all domains
457 (Figure 4E, Figure supplement 4C-D). When looking specifically at the L2 apical domain, where the SMC
458 differentiates, we noticed an increased relative frequency of CYCB1.1db-GFP expression specifically in

459 *kat* SMC neighbors at stage 0-II, whereas it decreases at stage 1-II (Figure 4F, Figure supplement 4E).
460 This is in stark contrast with SMC neighbors in wild-type primordia displaying first a relative mitotic
461 quiescence at stage 0-II, then enhanced mitotic activity at stage 1-II. Yet, in the SMC, no mitotic activity
462 increased was observed in *kat* as compared to wild-type primordia (Figure 4F, Figure supplement 4E).

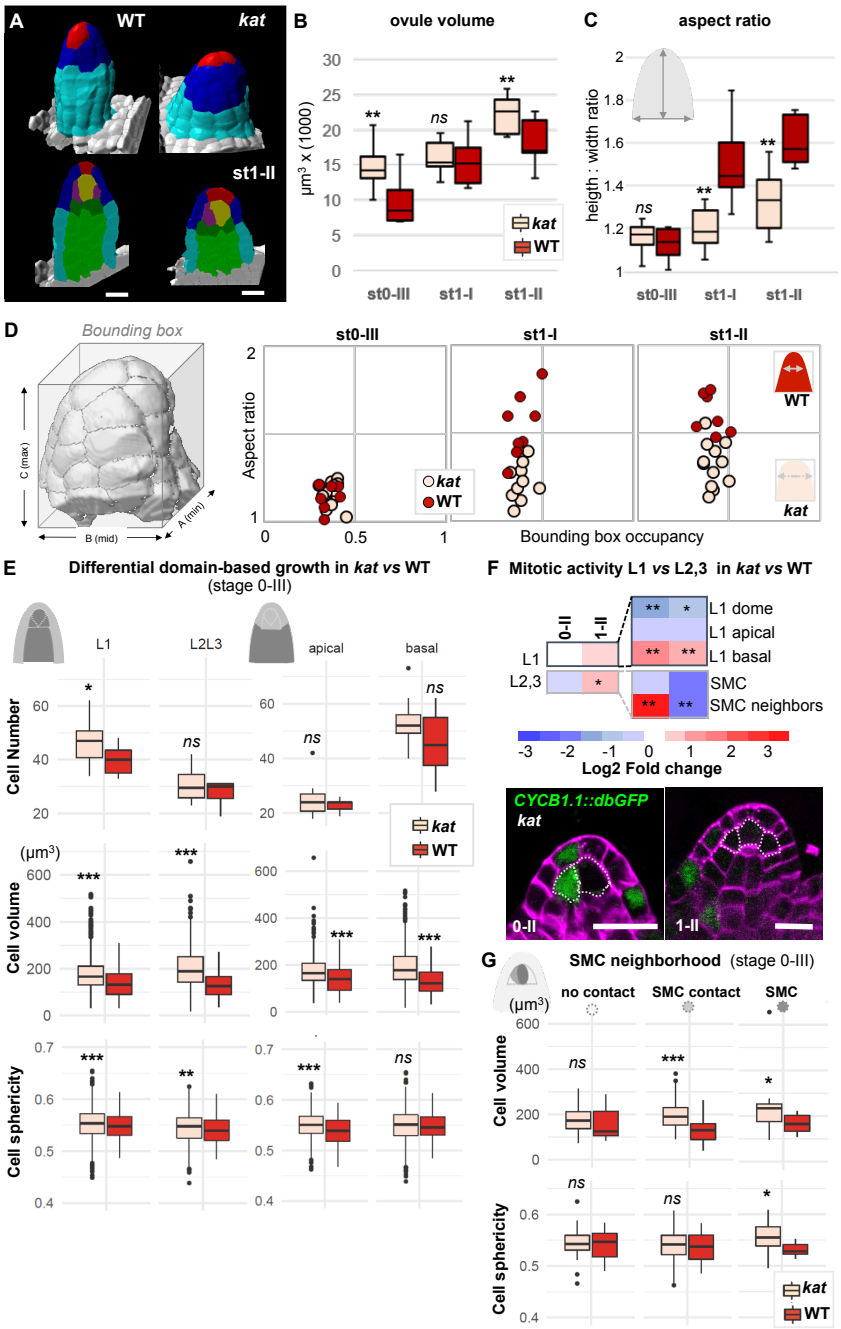

463 **Figure 4. *katanin* mutants show a distinct ovule primordium geometry.**

464 Comparison between wild-type (WT, Ws-4 accession) and *katanin (kat, bot1-7* allele*)* ovule primordia.
465 (A) 3D segmented images at stage 1-II. External organ view (top) and longitudinal sections (bottom) are shown.
466 Scale bar 10µm. See Source Data 2A for full datasets.

467 **Figure 4. *katanin* mutants show a distinct ovule primordium geometry (*continued*).**
468 (B-D) Morphological difference between WT and *kat* primordia measured by their volume (B), the aspect ratio (C),
469 and aspect ratio to bounding box occupancy relationship (D). D, Left: scheme representing the bounding box
470 capturing the primordium's 3D surface. See also Figure supplement 4A.
471 (E) Quantification of cell number, cell volume, and sphericity in comparisons of L1 *versus* L2,L3 and apical *versus*
472 basal domains at stage 0-III. See also Figure supplement 4C.
473 (F) Mitotic activity domains are altered in *kat* primordia. Top: Heatmap of Log2 fold change of mitotic activity in
474 the *kat* mutant (*lue1* allele) *versus* WT (Col-0) *per* domain, at two developmental stages. The frequency of mitoses
475 was measured as in Figure 2. Full maps of mitotic activity in different mutant alleles are shown in Figure
476 supplement 4E. Bottom: representative images of *kat* primordia (*lue1* allele) expressing CYCB1.1db-GFP. Dashed
477 lines mark L2 apical cells. Magenta signal: Renaissance SR2200 cell wall label. Scale bar 10µm.
478 (G) Mean cell volume and sphericity are increased in *katanin* L2 apical cells in contact with the SMC. SMC, cells in
479 contact with the SMC, and cells not in direct contact with the SMC, are compared at stage 0-III.
480 Color code in all plots: Dark red: WT; Salmon: *kat* mutant. Error bars: standard error of the mean. Differences
481 between WT and *kat* mutants in (B), (C), (E), and (G) were assessed using a Mann Whitney U test; a two-tailed
482 Fischer's exact test was used in (F). P values: *p≤0.05, **p≤0.01, ***p≤0.001. See also Figure supplement 4 and
483 Source Data 4.
484

485 In conclusion, the absence of *KATANIN*-mediated cell growth anisotropy is associated with
486 spatio-temporal shifts in cell divisions leading to an altered primordium geometry including a flatter
487 dome and enlarged basis. Interestingly, this coincided with the occurrence of additional large cells in the
488 L2 apical domain of *kat* primordia (SMC direct neighbor cells, Figure 4G, Materials and Methods) similar
489 in size to the SMC. This raises the question of the identity of these ectopic, enlarged cells.
490

491 **Altered ovule primordium geometry in *katanin* mutants induces ectopic SMC fate**
492

493 Following the observation of misshaped *kat* primordia and coinciding with larger L2 apical cells,
494 we asked whether this had an impact on cell identity and SMC establishment. Like in wild-type, a clear
495 SMC is identifiable in *kat* primordia yet it appears slightly bigger and more spherical with some
496 variability over stages (Figure 5A, Figure supplement 5A). Interestingly, and consistent with the
497 increased mitotic frequency in SMC neighbors observed at earlier stages, at stage 1-II, we scored
498 additional SMC neighbors in *kat* primordia, that were on average larger (14%, P=0.006) and slightly more
499 isotropic in shape (~11% less ellipsoid P=0.03, ~2% more spherical, P<0.01) than in the WT (Figure 5B).
500 At stage 1-II, 34% *kat* primordia (n=109) showed more than one enlarged, subepidermal cell; decreasing
501 to 14.4% at stage 2-II (n=104), in stark contrast with wild-type primordia showing a majority (86 to 96%)
502 of primordia with an unambiguous, single SMC (Figure 5C). The *kat* phenotype is thus reminiscent of
503 mutants affecting SMC singleness (Pinto et al., 2019) and we hypothesized that these enlarged cells
504 could be ectopic SMC candidates.

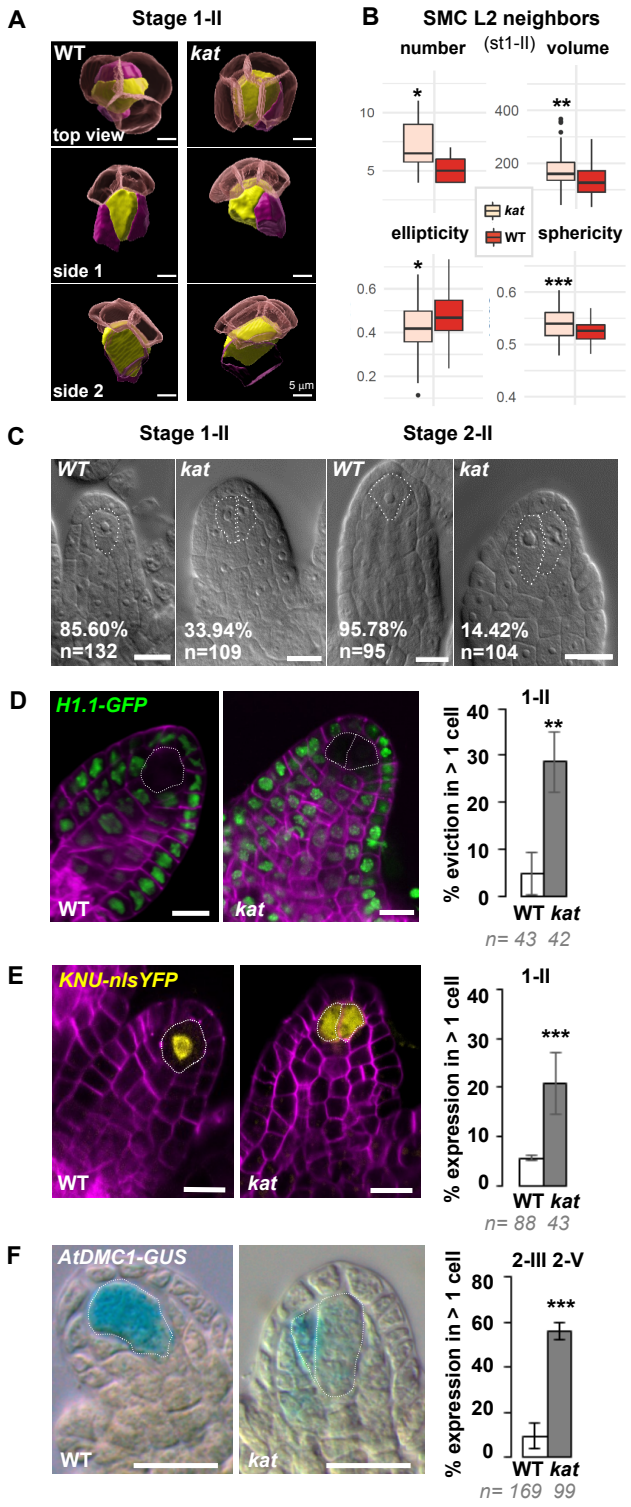

Figure 5. Altered ovule primordium geometry in *katanin* mutants is associated with multiple SMCs.

(A) SMCs lose their typical pear shape in *katanin* (*kat*) mutants. 3D images of the apical-most cells according to top and side views as indicated, showing the SMC (yellow), SMC neighbors (purple), and the L1 dome (transparent red).
(B) Differential properties of L2,L3 apical domain cells (SMC and SMC neighbors) in terms of cell number, mean cell volume, ellipticity, and sphericity at stage 1-II. See also Figure supplement 5A and Source Data 4B.
(C) Representative images of cleared wild-type (WT) and *kat* ovule primordia. The % indicate the frequency of ovules showing one SMC for WT primordia, or multiple SMC candidates (dashed lines) for *kat* primordia.
(D-E) Representative images and quantification of SMC fate markers in WT and *kat* primordia: eviction of the *H1.1::H1.1-GFP* marker (green, D) and ectopic expression of *KNU::nls-YFP* (yellow, E) in more than one cell *per* primordia, are increased in *kat* primordia. See also Figure supplement 5B.
(F) The meiotic marker *AtDMC1::GUS* is ectopically expressed in *kat* ovules.

Mutant alleles: *bot1-7* (A-B), *mad5* (C-E), *lue1* (F). Additional *kat* alleles, stages and detailed quantifications are presented Figure supplement 5 and Source Data 5. Magenta signal in (B) and (C): Renaissance SR2200 cell wall label. Scale bars for (A): 5 µm ; for (C), (D), (E), (F): 10µm. n: number of ovules scored. Error bar: standard error of the mean. Differences between WT and *kat* genotypes were assessed using a Mann Whitney U test in (B), and a two-tailed Fischer's exact test in (C), (D), (E), and (F). P values: *p≤0.05, **p≤0.01, ***p≤0.001. See also Figure supplement 5 and Source Data 5.

To verify this hypothesis, we introgressed several markers of SMC identity in *kat* mutant alleles. The first marker is a GFP-tagged linker histone variant (H1.1-GFP) that marks the somatic-to-reproductive fate transition by its eviction in the SMC at stage 1-I (She et al., 2013). H1.1-GFP eviction

509 occurred in more than one cell in 28.6% of *kat* primordia (n=43, Figure 5D). The second marker reports
510 expression of the *KNUCKLES* transcription factor (KNU-YFP) in the SMC (Tucker et al., 2012). Detectable
511 as early as stage 1-I in the wild type, it was ectopically expressed in 21% of *kat* primordia at stage 1-II
512 (n=43) (Figure 5E, Figure supplement 5B). Third, to test whether the ectopic SMC candidates have a
513 meiotic competence, we analyzed the AtDMC1-GUS reporter (Agashe et al., 2002; Klimyuk et al., 1997),
514 and indeed scored ectopic expression in 57% of *kat* primordia (n=56) (Figure 5F). We also analyzed the
515 *pWOX2-CenH3-GFP* marker labeling centromeres starting at the functional megaspore stage (De Storme
516 et al., 2016) and found 20.7% *kat* primordia (n=29) with two labeled cells, as compared to 3.8% (n=26) in
517 the wild type (Figure supplement 5C).

518 Taken together, these results show that ectopic, abnormally enlarged SMC neighbors in *kat*
519 primordia show at least some characteristics of SMC identity, and ectopic spores are also observed,
520 indicating that reproductive fate is altered in *kat* ovule primordia.
521

522 **SMC singleness is progressively resolved during primordium growth**

523 Based on our analysis of *kat* primordia, it appeared that the frequency of ectopic SMC
524 candidates was high at early stages but decreased over time (Figure 5C). This is reminiscent of the
525 phenotypic plasticity in SMC differentiation observed, to a lesser degree, in different *Arabidopsis*
526 accessions (Rodriguez-Leal et al., 2015). To characterize this plasticity during development we analyzed
527 1276 wild-type primordia from stage 0-II to 2-II and scored the number of primordia with one or two
528 enlarged, centrally positioned, subepidermal cells (class A and B, respectively, Figure 6A-C). In the wild
529 type, the majority of ovules showed a single candidate SMC (class A) at stage 0-II but 27% of primordia
530 (n=289) had two SMC candidates (class B), this frequency decreasing to 3% at stage 2-II (n=103). This
531 finding is consistent with ~ 5% primordia in wild-type at stage 1-II showing H1.1-GFP eviction (n=43) and
532 KNU-YFP expression (n=88) in more than one cell, respectively (Figure 5D-E). Thus, instead of being
533 immediate, SMC singleness can arise from a progressive restriction of fate among several SMC
534 candidates during development. In wild-type primordia, SMC singleness is largely resolved at stage 1-I
535 (Figure 5E).
536
537
538
539
540
541

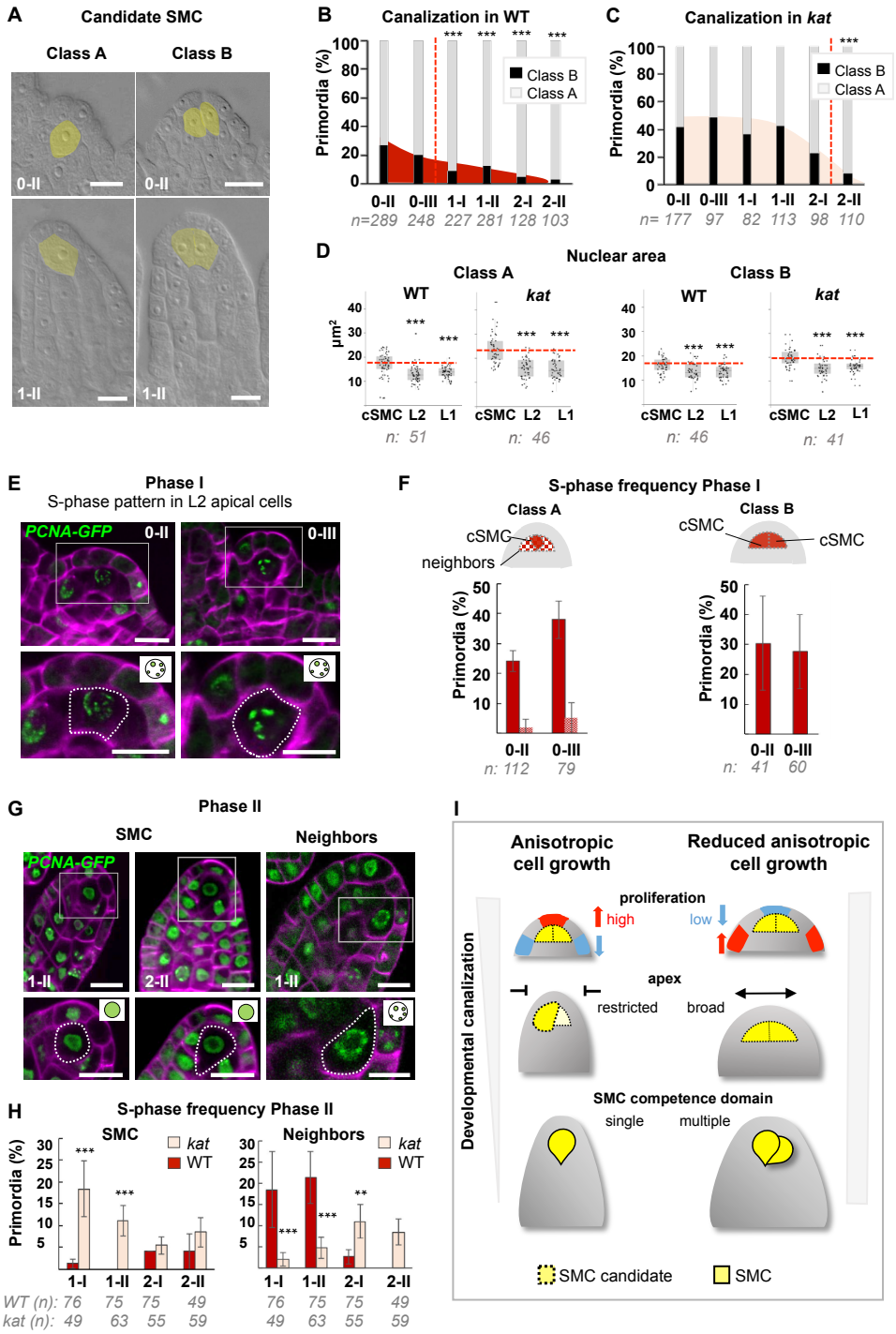

Figure 6. SMC singleness is progressively resolved during primordium growth.

(A-B) In wild-type (WT) plants, ovule primordia harbour one (class A) or occasionally two (class B) SMC candidates with the frequency of class B gradually decreasing during development, reminiscent of developmental canalization. Typical images obtained by tissue clearing with SMC candidates highlighted in yellow (A) and plots showing the percentages of classes A and B (B). The frequency of class B ovules is significantly reduced from stage 1-I, suggesting that canalization (represented by the red dashed line) occur before that stage. The plot coloration is a visual aid only.

550 **Figure 6. SMC singleness is progressively resolved during primordium growth (*continued*).**

551 (C) Developmental canalization is delayed in *katanin* mutants (*kat*, *mad5* allele). The proportion of class B ovules is
552 significantly reduced from stage 2-II only. Quantifications for two additional mutants carrying *kat* alleles are
553 presented Figure supplement 6A. The plot coloration is a visual aid only.
554 (D) The candidate SMCs initially identified as enlarged cells consistently show an enlarged nucleus in both class A
555 and class B primordia. Nuclear area is compared between the candidate SMCs (cSMC) and surrounding L2 and L1
556 cells (see Figure supplement 6D and Materials and Methods for further details). Box plots include jittered data
557 points to visualize data variability. Red lines represent the median of cSMC nuclear area for comparison with other
558 cell types. Equivalent quantifications for stage 0-III are presented in Figure supplement 6E.
559 (E-F) During Phase I (stages 0-II, 0-III), S-phase is detected in candidate SMCs at higher frequency than in neighbors
560 cells in class A ovules, and in both SMC candidates in class B ovules. Representative images of ovule primordia
561 showing the speckled S-phase pattern of the *pPCNA1::PCNA1:sGFP* reporter (green) (E). Magenta signal:
562 Renaissance SR2200 cell wall label. Scale bar 10µm. Quantification of speckled S-phase pattern in the SMC
563 candidate and L2 neighbors (class A ovules) or in both SMC candidates (class B) (F).
564 (G-H) During Phase II (stages 1-I to 2-II), in class A wild-type ovule primordium, SMC exits S-phase, and neighbors
565 cells undergo S-phase; while *katanin* primordia show the opposite pattern. Representative images of class A ovule
566 primordia primarily showing the nucleoplasmic pattern of *pPCNA1::PCNA1:sGFP* in SMCs at stages 1-II (left panel)
567 and 2-II (middle panel); and of the speckled S-phase pattern in neighbors cells (right panel). Quantification of
568 speckled S-phase pattern in SMC candidates and neighbors in Phase II wild-type and *katanin* primordia (I).
569 Representative images and quantifications of Phase I *katanin* primordia and of class B primodia are presented in
570 Figure supplement 6F-H. See also Figure 2H.
571 (I) Model for the role of *KATANIN* in primordium growth and SMC differentiation (graphical abstract). In WT
572 primordia, SMC differentiation follows a developmental canalization process influenced by cell growth anisotropy
573 that shapes the primordium apex. In *kat* mutants, reduced anisotropy modifies the cell proliferation pattern,
574 enlarges the apex and the L2,L3 apical domain, leading to multiple SMC candidates (delayed canalization). We
575 propose that ovule primordium shape, controlled by anisotropic cell growth, determines SMC singleness.
576 *Images*: scale bars : 10um. *Graphs*: n= total number of ovules. Error bar: standard error of the mean (F, I).
577 Differences between cell types, domains, or genotypes as indicated in the graphs were assessed using *Wilcoxon*
578 *signed rank test in (D), and* a two-tailed Fischer's exact test in B, C, F, and I. P values: *p≤0.05, **p≤0.01,
579 ***p≤0.001. Quantifications for additional alleles and detailed quantifications are provided in Figure supplement 6
580 and Source Data 6.
581

582 Next, we quantified class A and B primordia in *kat* mutants by scoring 2587 ovules of three
583 different mutant alleles (Figure 6C, Figure supplement 6A). Clearly, plasticity is more strongly expressed
584 with 42% (n=202) class B primordia at stage 0-II in *kat* compared to 26% (n=289) in the wild-type. In
585 addition, the resolution process is delayed in *kat* mutant primordia as up to 33% class B primordia
586 persist at stage 1-II (n=113) compared to 12% in the wild type (n=281). Consistently, the two SMC
587 markers used previously, clearly identify ectopic SMC candidates in *kat* primordia at stage 1-I (Figure
588 supplement 6B-C), and more significantly at stage 1-II (28.5% ectopic eviction of H1.1-GFP and 21%
589 ectopic expression of KNU-YFP, Figure 5D-E). In addition, at stage 2-II, when 17% of cleared *kat*
590 primordia (n=110) showed ectopic SMCs, H1.1-GFP eviction and KNU-YFP expression was only found in

591 8% (n=25) and 6.7% (n=74) of the primordia, respectively (Figure supplement 5B-C). Therefore,
592 molecular events associated with SMC fate are partially uncoupled from cell growth during the
593 resolution of SMC singleness in *kat*.

594 Another outcome of this study is the early emergence of SMC candidates, based on cell size
595 mostly and confirming our former 3D cell-based analysis that showed increased cell volume of the L2,L3
596 apical cells already at stages 0-I/0-II (Figure 2J). To corroborate this finding using a different criterion,
597 we measured the nuclear area, which is a distinctive feature of SMCs (Rodriguez-Leal et al., 2015; She et
598 al., 2013). We compared the nuclear area of SMC candidate to that of surrounding L1 and L2 cells, in
599 both class A and B primordia, at stages 0-II and 0-III. Wild-type class A and B primordia showed an
600 enlarged nucleus in the candidate SMCs from stage 0-II onwards, and this correlation was also true in
601 *kat* primordia (Figure 6D, Figure supplement 6D-E).

602 It remains however difficult to resolve the precise timing of SMC establishment at these early
603 stages due to the lack of molecular markers. Yet, we rationalized that we may distinguish the SMC
604 candidates from their neighbors by their cell cycle pattern, where cells entering meiosis may engage in a
605 specific S-phase compared to regularly cycling mitotic cells. To this aim, we used a GFP-tagged PCNA
606 variant marking the replication machinery, *pPCNA1::PCNA1:sGFP* (PCNA-GFP) (Yokoyama et al., 2016).
607 When engaged at active replication forks, PCNA-GFP shows nuclear speckles characteristic of S-phase
608 (Strzalka et al., 2011). During G1/G2, it remains in the nucleoplasm; and is undetectable in M-phase. We
609 specifically quantified the distribution patterns of PCNA-GFP in cells from the L2 apical domain in wild
610 type and *kat* primordia, separately for class A and B ovules (Figure 6E-H). In Phase I wild-type primordia,
611 PCNA-GFP was always detectable, in both classes, indicating that L2 apical cells are rarely in M-phase,
612 consistent with the seldom detection of mitoses using CYCB1.1db-GFP. We observed an S-phase pattern
613 consistently in one (Class A) or more (Class B), centrally positioned L2 apical cells, presumably
614 corresponding to SMC candidates (Figure 6E). This pattern was captured in a large proportion of
615 primordia at stage 0-II and 0-III: ~24% (n=112) and ~40% (n=79) respectively for class A; 30% (n=41) and
616 28% (n=60) for Class B, respectively (Figure 6F). Such high frequencies could be generated either by a
617 slow S-phase in SMCs candidate only (the persistence of the marker increasing the probability to score it
618 repeatedly in our sample size), or by a regular (short) mitotic S-phase in a high number of SMC
619 candidates. The low detection frequency of the mitotic marker CYCB1.1db-GFP in SMC candidates allow
620 rejecting the latter possibility. Thus, the likeliest interpretation is that candidate SMCs enter a slow S-
621 phase from early stages onwards, probably meiotic, although this cannot be assessed with this marker.
622 In *kat* primordia at Phase I, Class A ovules showed a wild-type pattern in the SMC at stage 0-II, but a

623 reduction at stage 0-III, suggesting alterations in S-phase entry; and class B ovules, by contrast, displayed
624 high frequency of S-phase pattern, which indicate either longer S-phase or multiple dividing cells (Figure
625 supplement 6G).

626 In Phase II, SMC candidates showed absence of S-phase pattern in a large majority of both Class
627 A and B primordia (96,6% on average, over all Phase II) (Figure 6G-H, Figure supplement 6G-H) in
628 agreement with the presence of newly replicated DNA at stage 1-I (She et al., 2013). By contrast with
629 Phase I, however, S-phase is now detected in SMC neighbors (~21% at stage 1-II) (Figure 6G-H)
630 consistent with the divisions observed in these cells (Figure 2D). Strikingly in Phase II, *kat* primordia
631 display a higher frequency of S-phase patterns in SMC candidates (Figure 6H, Figure supplement 6F,H),
632 suggesting that S-phase duration or entry timing is delayed compared to wild type. SMC neighbors, by
633 contrast, show a lower frequency of S-phase patterns (Class A), consistent with reduced division in these
634 cells (Figure 4F).

635 Collectively, our data indicate a cellular heterogeneity in terms of size, nuclear size and S-phase
636 patterns, of the L2 apical domain as compared to L1, which leads to the emergence of one or several
637 SMC candidates as early as stage 0-II. The gradual decrease in the number of primordia with ambiguous
638 SMC candidates demonstrates a developmentally-regulated resolution of SMC fate to a single cell. This
639 process is associated with a specific cell-cycle progression, cellular elongation, and robust expression of
640 SMC fate markers. In *kat* primordia displaying geometry alterations, SMC singleness is largely
641 compromised: plasticity in SMC emergence is increased and fate resolution to a single SMC is delayed.

642 **Discussion**

643

644 Organogenesis involves coordinated cell division and cell expansion, complex growth processes
645 orchestrated by biochemical and mechanical cues (Echevin et al., 2019). How cell differentiation is
646 coordinated in space and time during organ growth and whether these processes are interrelated are
647 central aspects for the elucidation of patterning principles (Whitewoods et al., 2017). The female
648 germline is initiated with SMC differentiation in the ovule primordium. The SMC emerges as a large,
649 elongated subepidermal cell that is centrally located at the apex of the primordium, a digit-shaped organ
650 emerging from the placenta. To study how SMC fate relates to ovule organogenesis, we generated a
651 reference collection of images capturing ovule primordium development at cellular resolution in 3D and
652 determined cell division frequencies in the different domains. We observed a biphasic pattern of cell
653 divisions alternating in the epidermis and inner layers, as well as the apical and basal domains, in Phase I
654 (stages 0-I to 0-III) and Phase II (stages 1-I to 2-II).

655 However, this approach did not allow us to resolve the driving morphogenetic factors. For this
656 reason, we developed continuous and cell-based 2D simulations of primordium growth. The different
657 simulations revealed key growth principles shaping the ovule primordium and uncovered differential
658 roles for the epidermis and inner layers. Notably, an inner tissue-driven growth model, where the L1
659 also contributes expansion of the primordium, best described ovule primordium growth. This is
660 reminiscent of the possible model describing leaf primordium emergence (Peaucelle et al., 2011) . In
661 addition, best-fit models produced by both cell-based and FEM simulations predicted a growth-
662 promoting signal in a confined domain along a vertical stripe at primordium emergence. Candidates
663 growth signals are phytohormones, peptides, and small RNAs known to affect ovule primordium growth
664 (Kawamoto et al., 2020; Pinto et al., 2019; Su et al., 2020). The domain of auxin response restricted in
665 the L1 dome and of cytokinin signaling localized in a region basal to the SMC in Phase II primordia
666 (Bencivenga et al., 2012) also suggest a confined growth signal. Whether the signaling domains are
667 established already in Phase I and plays a causative role in primordium patterning remains to be
668 determined. The epidermis, by contrast, is predicted to play a key role in accommodating the
669 constraints generated by inner-tissue growth. In this layer, passive strain-based growth and anisotropic
670 material properties possibly resolve mechanical conflicts arising between tissue layers that grow at
671 different rates (Hervieux et al., 2017). In line with this hypothesis, we observed frequent divisions in L1
672 apical cells *in vivo* that support the expansion of the epidermis while inner-tissues develop.
673 Interestingly, while our models did initially not contain an *a priori* rule to produce the typical,
674 elongated shape of the SMC, it emerged consistently as a trapezoidal-shaped L2 cell in the cell-based
675 reference model. This shape likely emerges from the combination of assigned anisotropic cell growth
676 and geometrical constraints imposed by the surrounding growing tissues. Explicitly blocking SMC
677 division during the simulation not only enabled its expansion as expected, but also pushed surrounding
678 cells and strongly deformed ovule morphology. Thus, ovule growth homeostasis *in vivo* likely requires a
679 mechanism to accommodate the differential growth of the SMC. A gradual reduction of SMC turgor
680 pressure is a plausible scenario that would limit SMC size and prevent overriding the constraints
681 provided by surrounding cells, similarly to what was suggested for the shoot apical meristem (Long et
682 al., 2020). In turn, a gradient of pressure in field of cells could provide positional information through
683 the directional movement of water and other molecules thereby linking organ growth homeostasis, cell
684 growth, and cell fate (Beauzamy et al., 2014; Long et al., 2020). Such a mechanism could also participate
685 in determining the domain of the growth-signal predicted by our simulations.
686

687 Another prediction of our growth models is the key role of anisotropic cell growth in controlling
688 the geometry of the ovule primordium. Primordia of the *katanin* (*kat*) mutant, deficient in the
689 microtubule severing enzyme KATANIN (Luptovciak, Komis, et al., 2017) resemble virtual mutant
690 primordia generated by models where cell growth is isotropic in the inner layers. *kat* primordia have a
691 flatter dome and large basis associated with global alterations in cell proliferation pattern, cell size and
692 cell shape. Interestingly, *kat* primordia develop ectopic SMC candidates as early as stage 0-II. The most
693 parsimonious hypothesis is that the altered geometry in *kat* primordia expands the domain of cells
694 competent to form SMCs. Yet, we cannot exclude a direct effect of the *kat* mutation on L2 apical cells,
695 disconnected from organ geometry, which would induce *de novo* SMC fate. However, this scenario is
696 unlikely because we would expect increased cell growth and slower mitoses (Luptovciak, Komis, et al.,
697 2017), resulting in a reduced division frequency of L2 apical cells, which is not the case. Instead, we
698 measured increased cell divisions in L2 SMC neighbors at stage 0-II. Also, the delayed divisions of SMC
699 neighbors in *kat* at stage 1-II cannot explain the formation of ectopic SMC candidates at stage 0-II.
700 Therefore, the most parsimonious explanation is that the emergence of several SMC candidates in *kat*
701 primordia is an effect of ovule primordium geometry. In this scenario, isotropic cell growth and altered
702 mechanical constraints in the tissue acting from primordia emergence onwards, lead to divisions and
703 patterning alterations expanding the domain of cells competent for SMC fate. This working model paves
704 the way to explore the role of the epidermis geometry in controlling regulators of cell cycle and SMC
705 fate in L2 apical cells. This is reminiscent to the shoot apical meristem epidermis acting on dome shape
706 and stem cells regulators in underlying layers (Gruel et al., 2016; Savaldi-Goldstein et al., 2007). The
707 predicted role of the primordium epidermis to accommodate - and perhaps feedback on – underlying
708 growth constraints is particularly interesting considering the role of mechanical cues on gene regulation
709 (Fal et al., 2017; Landrein et al., 2015). The epidermis of the ovule primordium is also a known source of
710 signaling cues (Kawamoto et al., 2020; Pinto et al., 2019; Su et al., 2020). In addition, phytohormones act
711 themselves on KATANIN-mediated oriented cell growth and cell division (Luptovciak, Komis, et al.,
712 2017). In this context, it is possible to speculate that misshaping of *kat* primordia may also arise from a
713 disrupted feedback altering the distribution pattern of the hypothesized growth signals.
714 Furthermore, our analyses unveiled new characteristics of the SMC establishment process. We
715 found that SMC candidates emerge from within a mitotically quiescent L2 apical domain, consistent with
716 the finding that the H3.1 histone variant HTR13 is evicted, marking cell cycle exit (Hernandez-Lagana et
717 al., 2020). In addition, SMC candidates have a markedly long S-phase compared to surrounding cells.
718 These observations are reminiscent of the animal germline where mitotic quiescence is a prerequisite to

719 meiosis (Kimble, 2011; Reik et al., 2015). Also, early SMC candidates already display a typically large cell
720 and nucleus size and an elongated shape aligned with the primordium growth axis. Collectively, we
721 found that SMC characteristics are established much earlier than previously thought, i.e. soon after
722 primordium emergence (stages 0-II /0-III). Moreover, these characteristics frequently arise in more than
723 one SMC candidate at Phase I, resolving into a single SMC at the onset of Phase II. This clearly
724 documents a developmental sequence of plasticity at SMC fate emergence and progressive resolution of
725 SMC fate in a single cell. This is reminiscent of developmental canalization, which refers to the capacity
726 of an organism to follow a given developmental trajectory in spite of disturbances (Hallgrimsson et al.,
727 2019; Scharloo, 1991; Waddington, 1942). Cell fate canalization is well studied in animal systems where
728 it is modulated by intercellular signal-based feedback mechanisms (Heitzler et al., 1991), epigenetic
729 regulation (Pujadas et al., 2012) and organ geometry (Huang et al., 2020; Huang, 1992; Pujadas et al.,
730 2012; Royer et al., 2020). In plants, canalization is better known in the context of organogenesis during
731 phyllotaxis and developmental robustness (Godin et al., 2020; Lempe et al., 2013). Our study expands
732 the examples of a canalization process at the level of a cellular domain, in the Arabidopsis ovule
733 primordium. While L2 apical cells initially share the competence to form SMC candidates, leading to
734 plasticity at SMC emergence, the progressive restriction of cell fate possibilities in the primordium apex
735 ultimately leads to only one SMC committed to meiosis. Our results are in line with a formerly proposed
736 canalization process operating during SMC establishment (Grossniklaus et al., 1998; Rodriguez-Leal et
737 al., 2015). Despite the fact that several mutations (Pinto et al., 2019; Mendes et al., 2020), including *kat*
738 (this study), alter SMC singleness, canalization remains a robust process securing the formation of a
739 single embryo sac for most of these genetic perturbations in Arabidopsis. How this developmental
740 mechanism buffers phenotypic inter-individual variations and whether it is evolutionary constrained
741 remains to be determined.

742 In this study, we quantified plasticity among ovule primordia and progressive fate resolution
743 during primordium growth in wild-type reference accessions. We characterized specific cellular events
744 associated with these processes, notably differential cell growth and cell division. SMC fate emergence is
745 characterized by mitotic quiescence and cellular growth in one or more L2 apical cells. SMC singleness
746 resolution is associated with re-entry in a somatic cell cycle (this study), and re-incorporation of a
747 replicative histone H3.1 (Hernandez-Lagana et al., 2020) of initial candidates neighboring the SMC. How
748 known epigenetic and signaling factors interplay to secure SMC singleness remains to be determined.
749 Similar to mouse and Drosophila, where tissue mechanics and organ geometry were shown to
750 contribute to cell fate canalization (Chan et al., 2017; Huang et al., 2020; Royer et al., 2020), we propose

751 that ovule primordium geometry contributes to channel SMC fate in the apex and to the resolution of a
752 single SMC. In this conceptual framework, *kat* increases plasticity and delays the resolution process
753 towards SMC singleness (working model Figure 6I).

754 Altogether our work proposes a conceptual framework linking organ geometry, cell shape and
755 cell fate acquisition in the ovule primordium, potentially of broader relevance in plant patterning. In
756 addition, the image resource published in this study is complementary to others capturing ovule
757 development at later stages (Lora et al., 2017; Vijayan et al., 2020). It also populates a growing number
758 of 3D-segmented images of plant tissues and organs (Wolny et al., 2020), which collectively build the
759 fundaments to developmental atlas integrating morphogenesis with gene expression (Hartmann et al.,
760 2020).

761

762

763 # Materials and Methods

764 **Key Resources Table**

REAGENT or RESOURCE	SOURCE	IDENTIFIER
Chemicals		
SCRI Renaissance Stain 2200	Renaissance Chemicals	http://www.renchem.co.uk/index.php/specialty-chemicals-division/item/48-selected-fluorescent-dyes-and-brighteners-for-microscopists
Propidium Iodide (mPS-PI staining solution)	Sigma- Aldrich	Catalog # P4170
Sodium metabisulphite (mPS-PI staining solution)	Sigma- Aldrich	Catalog # S9000 / PubChem: 329824616
Deposited Data		
Images dataset 3D segmentation ovule primordium wild-type (*Col-0, Ws-4*) and *katanin* mutant (*bot1-7* allele)	This paper, *submission to IDR repository underway*	https://idr.openmicroscopy.org/
Experimental Models: Organisms/Strains		
Arabidopsis thaliana, ecotype Col-0	NASC	NASC ID: N22625
Arabidopsis thaliana, ecotype Ws-4	NASC	NASC ID: N5390
Arabidopsis thaliana, *bot1-7* mutant	H.Höfte, (Bichet et al., 2001)	
Arabidopsis thaliana, *mad5* mutant	O.Voinnet (Brodersen et al., 2008)	
Arabidopsis thaliana, *lue1* mutant	(Bouquin et al., 2003); NASC	NASC ID: N57954
Arabidopsis thaliana, *promCYCB1.1::CYCB1.1db-GFP*	M.Bennett (Ubeda-Tomas et al., 2009)	
Arabidopsis thaliana, *promH1.1::H1.1-GFP*	(She et al., 2013)	
Arabidopsis thaliana, promKNU::nls-YFP	M.Tucker (Tucker et al., 2012)	
Arabidopsis thaliana, promAtDMC1::AtDMC1-GUS	I.Siddiqi (Klimyuk et al., 1997)	
Arabidopsis thaliana, promWOX2::CenH3-GFP	N.DeStorme (De Storme et al., 2016)	
Arabidopsis thaliana, promPCNA1::PCNA1-GFP	S. Matsunaga (Yokoyama et al., 2016)	
Software and Algorithms		
IMARIS Cell	Bitplane, AG	https://imaris.oxinst.com/
ExportImarisCells, plugin for IMARIS	This paper	https://github.com/barouxlab/ExportImarisCells
MorphoGraphX	Freely available	http://www.mpipz.mpg.de/MorphoGraphX
MorphoMechanX	Freely available	https://www.mpipz.mpg.de/MorphoGraphX/MorphoMechanX/
MassSpringModels_ovuleGrowth2D, plugin for MorphoMechanX	This paper	https://github.com/GabriellaMosca/MassSpring_2DovuleGrowthModel
FEM_2DOvuleGrowthModel, plugin for MorphoMechanX	This paper	https://github.com/GabriellaMosca/FEM_2DOvuleGrowthModel
3DAutoLabeling-ShapeQuant, plugin for MorphoMechanX	This paper	https://github.com/GabriellaMosca/3DAutoLabeling-ShapeQuant
OvuleViz, R-based data plotting interface	This paper	https://github.com/barouxlab/OvuleViz
R / RStudio	Freely available	https://www.r-project.org/ http://www.rstudio.com/.
OMERO	Freely available	https://www.openmicroscopy.org/omero/
ImageJ / FIJI	Freely available	https://imagej.net/Fiji

765

766 **Plant growth and plant material.**

767 *Arabidopsis thaliana* plants were grown under long-day conditions (16 hours light) at 20-23 C in a plant
768 growth room. Columbia (Col-0) and Wassileskija (Ws-4) accessions were used as wild-type controls
769 depending on the mutant background used in the experiment. Three *katanin* alleles were used: *bot1-7*
770 (Bichet et al., 2001) in Ws-4 accession, *lue1* (Bouquin et al., 2003) and *mad5* (Brodersen et al., 2008)
771 both in the Columbia (Col-0) accession. Homozygous mutant individuals for all the *katanin* alleles were
772 identified on the basis of their recessive vegetative phenotype. The following published markers were
773 used: pCYCB1.1:db-GFP (Ubeda-Tomas et al., 2009), pKNU:nls:YFP (Tucker et al., 2012), pH1.1:H1.1:GFP
774 (She et al., 2013), AtPCNA1:sGFP (Yokoyama et al., 2016), pAtDMC1:GUS (Agashe et al., 2002; Klimyuk et
775 al., 1997), pWOX2:CenH3:GFP (De Storme et al., 2016), and crossed to *katanin* mutants, and to Ws-4
776 ecotype for *bot1-7* allele comparisons.

777 **3D imaging and image processing (segmentation and labeling).**

778 Entire carpels were stained using the pseudo-Schiff propidium iodide (PS-PI) cell wall staining procedure
779 providing excellent optical transparency for 3D imaging in depth in whole-mount. We described
780 previously the manipulation, staining, mounting of the flower carpels and imaging procedures
781 (Mendocilla-Sato, 2017). Cell-boundary based image segmentation was done using ImarisCell (Bitplane)
782 as described in details previously (Mendocilla-Sato, 2017). Each ovule was manually labelled in Imaris
783 using customized Cell Labels for the different cell types and domains colored as shown in Figure 1**.** We
784 defined the labels as follows:

785 • SMC (Spore Mother Cell): most apical central enlarged L2 cell. At stage 0-I, as enlargement is not
786 always detected visually, the most apical L2 cell was then selected as candidate SMC (cSMC).
787 • L1: epidermal cells
788 • L1 dome: most apical cells in contact with SMC
789 • L2/L3: cells below the epidermis. L2 and L3 were not distinguished originally.
790 • Apical domain: group of cells at the apex of the primordium and encompassing the SMC and direct
791 neighbor cells.
792 • Basal domain: group of cells at the basis of the primordium below the apical domain and until, but
793 not including cells of the placental surface. At stages 0-I and 0-II only an apical domain is defined. A
794 basal domain appears only starting stage 0-III.
795 • CC (Companion Cell): L2 cells in apical domain in contact with the SMC with an elongated shape (as

796 judged in ovule longitudinal median section using the "clipping plane" IMARIS tool).

797 • SMC contact: cells in contact with the SMC.

798 Semi-automated segmentation requiring user input and manual labelling can be error prone. To reduce
799 the error rate, the 92 images were segmented and labeled by one author, but verified and curated by
800 two others. All Imaris files used in the study will be available at the IDR repository (www.idr.org).

801

802 **Ovule stage classification.**

803 Ovule development is described according to a well-accepted nomenclature (Schneitz, 1995). The first
804 stage, initially defined as stage 1-I, indistinctly grouped primordia from emergence until digit shape. To
805 enable describing early morphogenetic processes, however, we propose to (i) restrict stage 1-I to the
806 final digit shape stage and (ii) subdivide preceding stages as stages 0-I, 0-II and 0-III, as shown in Figure
807 1B. These developmental stages are classified according to the approximate number of cell layers
808 protruding above the placenta and overall shape of the ovule as described in Table 1 and Source Data 1.

809 **Quantification of cell number, size and shape and interactive plotting using OvuleViz.**

810 Several cell descriptors were retrieved using the ImarisCell' Statistics function and exported as .csv files:
811 cell area, cell volume, cell sphericity, cell ellipticity (oblate and prolate). We developed an interactive R-
812 based data plotting interface, OvuleViz, reading the Imaris-derived data within the exported files
813 ordered by genotype then stages (Figure supplement 1). OvuleViz is freely available at
814 https://github.com/barouxlab/OvuleViz, and is based on a *shiny* interface for R. OvuleViz allows plotting
815 selectively one or several of the cell descriptors for chosen stages and genotypes, along different
816 visualization (scatter plots, box plots, histograms). In addition, OvuleViz retrieves the cell number from
817 the number of objects in the .csv file.

818 **3D quantification of ovule volume and shape using IMARIS.**

819 Ovule volume and shape were quantified on 3D segmentations using IMARIS software, to compare
820 *katanin* and wild-type genotypes. For each ovule, all segmented labeled cells were duplicated and fused
821 as a single cell object. The *ImarisCell' Statistics* function was used to retrieve "cell volume" and
822 "bounding box OO" (object oriented 3D bounding rectangle, exporting the minimum (A), mid (B) and
823 maximum (C) lengths of the object bounding rectangle). Width to Height ratio was calculated by dividing
824 the maximum (C) length by the mean of mid (B) + minimum (A) lengths. Bounding box occupancy was
825 calculated as the ratio of ovule volume by the bounding box volume.

826 **Modeling and image analysis with MorphoMechanX.**

827 The details of tissue growth models and MorphoMechanX-based processing are described in
828 Supplemental File 1.

829 **2D cytological analysis of cleared ovule primordia and quantifications.**

830 For cytological examination of cleared ovule primordia, flower buds from wild-type and mutant plants
831 were harvested and fixed in formalin-acetic acid-alcohol solution (40% formaldehyde, glacial acetic acid,
832 50% ethanol; in a 5:5:90 volume ratio) for at least 24h at room temperature. After fixation, samples
833 were washed two times with 100% ethanol and stored in 70% ethanol. Gynoecia of 0.2–0.6 mm in
834 length were removed from the flowers with fine needles (1 mm insulin syringes), cleared in Herr's
835 solution (phenol : chloral hydrate: 85% lactic acid : xylene: clove oil in 1:1:1:0,5:1 proportions), and
836 observed by differential interference contrast microscopy using a Zeiss Axioimager Z2 microscope and
837 40X or 60X oil immersion lenses. Picture were acquisition was done with a sCMOS camera (Hamamatsu
838 ORCA Flash V2). Nuclei area measurements were carried out with ImageJ software, using the manual
839 contour tool "Oval".

840 **Fluorescence microscopy and quantifications.**

841 Imaging of ovule primordia stained in whole-mount for cell boundary was done as described
842 (Mendocilla-Sato, 2017) using a laser scanning confocal microscope Leica LCS SP8 equipped with a 63X
843 glycerol immersion objective and HyD detectors.

844 Imaging of the GFP and YFP markers was performed using a laser scanning confocal microscope Leica
845 LCS SP8 equipped using a 63X oil immersion objective and HyD detectors. Samples were mounted in 5%
846 glycerol with the cell wall dye Renaissance 2200 (SR2200) diluted 1/2000. The following wavelengths
847 were used for fluorescence excitation and detection: Renaissance: excitation 405nm, and detection
848 415–476 nm; GFP: excitation 488m and detection 493-550 nm; YFP: excitation 514nm and detection
849 590-620nm. Channels contrast and intensity were adjusted using ImageJ or OMERO.

850 The mitotic activity in both wild-type and *katanin* ovules was quantified by scoring the cells expressing
851 *promCYCB1::dbCYCB1-GFP* (M phase reporter) on 3D stacks, in each ovule domain at each
852 developmental stage. Only ovules showing at least one cell expressing *promCYCB1::dbCYCB1-GFP* were
853 included in the analysis. At a given stage, the frequency of mitoses per domain is the ratio between the
854 number of GFP positive cells within a domain in all observed ovules, to the total number of GFP positive
855 cells found in all domains in that population of ovules.

856 To quantify ectopic expression of H1.1-GFP, KNU-YFP and pWOX2:CenH3-GFP markers, the percentage
857 of ovules presenting expression (or eviction in the case of H1.1-GFP) of the marker in more than one cell
858 was scored on 3D stacks. To quantify PCNA-GFP patterns, using 3D stacks, cells of the L2 apical domain
859 were classified according to the "speckled" or "nucleoplasmic" patterns, or absence of the marker.

860 **Histochemical detection of *uidA* reporter gene product (GUS staining).**

861 Gynoecia of 0.4–0.6 mm in length were removed from the flowers with fine needles and placed in
862 staining solution, using high stringency conditions for ferro- and ferricyanide concentrations to limit GUS
863 product diffusion (0.1% Triton X-100, 10 mM EDTA, 5 mM ferrocyanide, 5 mM ferricyanide and 20mg/ml
864 5 -bromo-4-chloro-3-indolyl-beta-d-glucuronic acid cyclohexyl-ammonium salt (X-gluc, Biosynth AG,
865 Staad, CH) in 50 mM phosphate buffer), for 96h at 37°C. After staining, the samples were mounted in
866 clearing solution (50% glycerol, 20% lactic acid diluted in water) and observed by differential
867 interference contrast microscopy using a Zeiss Axioimager Z2 microscope. Picture acquisition was done
868 with a color sCMOS camera (Axiocam 503 color Zeiss).

869 **Statistical analysis.**

870 To identify the main cellular descriptors – cell area, cell volume, sphericity, ellipticity oblate, ellipticity
871 prolate – explaining variance of each cell types, at each ovule primordium growth stages and between
872 genotypes, we used principal component analysis (PCA) on a cells' descriptors matrix. PCA was executed
873 using the R software version 3.6.3. In all different subsets of data, PCA was performed by singular value
874 composition of the centred and scaled data matrix. Data entries with missing values were removed
875 before analysis. All Cell data as exported by Imaris were uploaded but only cells with a 'Cell Label' as
876 described in the method section '3D imaging' were plotted. For visualization of PCAs, only the first two
877 principal components were represented in both score and loading plots.

878 To determine if the means between two datasets were significantly different we used two-tailed t-test
879 when the data were normally distributed (n> 30). For all datasets with n <30, we assume that normality
880 was not possible to assess properly (as small samples most often pass normality tests), thus we used
881 non parametric tests. Wilcoxon Signed-Rank two-tailed test was used for paired quantifications, and
882 Mann Whitney U two-tailed test was used for unpaired quantifications. Tests were performed in Excel or
883 in R (wilcox.test function). To compare ovule proportions, we used two-tailed Fischer's Exact test, using
884 https://www.langsrud.com/fisher.html, available online. Variability was assessed using the Standard
885 Error of the mean (SE), indicated in the graphs and/or the supplemental data when applicable. For some

886 datasets, boxplots were used to improve visualization of data distribution. The number of samples and
887 biological replicates for each experiment are indicated in the figure and/or figure legends and/or
888 supplemental data.

889 Author contributions

890 CB, DA, GM, EHL, DG, OH, AB, CG: Conceptualization; EHL, GM, CB, DA, OH, AB, CG, DG: Methodology;
891 GM, NP, AG: Softwares; EHL, GM, EMS, DA, CB: Validation; EHL, GM, AG, DA, CB: Formal analysis; EHL,
892 EMS, DA, CB: Investigation; EMS, AF, OH: Ressources; EHL, GM, NP, DA, CB: Data curation; EHL, GM,
893 EMS, DG, DA, CB: Writing – Original Draft; EHL, GM, OH, AB, CG, UG, DG, DA, CB: Writing – Reviewing
894 and Editing; EHL, GM, DA, CB: Visualization; CB, DA, DG, OH, AB, UG: Supervision; CB, DA, DG: Project
895 administration; CB, DA, DG, OH, AB, CG, UG: Funding Acquisition. All authors reviewed and revised the
896 manuscript.

897 Data availability

898 All materials, scripts and datasets generated and analyzed in the current study are available at
899 repositories (see Materials and Methods) or from the corresponding authors upon reasonable request.

900 Acknowledgments

901 We thank S. Strauss (Max Planck Institute for Plant Breeding Research, Cologne, Germany) and B. Lane
902 (John Innes Centre, Norwich, U.K.) for providing code and assessment for mesh generation and
903 simulations; S. Guyer (Bitplane, Switzerland) and M. Lartaud (CIRAD, France) for their help with IMARIS
904 analyses; O. Leblanc (IRD Montpellier, France) for his help with data visualization in R; the Montpellier
905 imaging facility MRI, member of the national infrastructure France-BioImaging supported by the French
906 National Research Agency (ANR-10-INBS-04) and the Center for Microscopy and Image Analysis of the
907 University of Zurich (ZMB) for microscopy imaging infrastructures; M. Ueda (Nagoya University, Japan),
908 I. Siddiqi (Center for Cellular and Molecular Biology, India), N. de Storme (Katholieke Universiteit Leuven,
909 Belgium), S. Matsunaga (Tokyo Science University, Japan), M. Tucker (University of Adelaide, Australia),
910 and the NASC stock center for seed germplasms.

911 This work was funded by the University of Zürich, the IRD, a PRCI grant from the Agence Nationale de la
912 Recherche/Swiss National Science Foundation (#ANR-16-CE93-0002) to CB and DA; grants from the
913 Swiss National Science Foundation (# 310030B_160336 to UG, # IZCOZ0_182949 to CB), from the
914 Commission for Technology and Innovation (CTI grant #16997) to CB, from the Baugarten Stiftung Zürich
915 to CB, a CONACYT fellowship (# 438277) to EHL, and a fellowship from the Forschungskredit of the
916 University of Zurich (#FK-74502-04-01) to GM.

Conflict of interest

The authors declare no conflict of interest.

References

Agashe, B., Prasad, C. K., & Siddiqi, I. (2002). Identification and analysis of DYAD: a gene required for meiotic chromosome organisation and female meiotic progression in Arabidopsis. *Development, 129*(16), 3935-3943.

Amar, M. B. G., A.; Müller, M.M.; Cugliandolo, L. . (2011). *New Trends in the Physics and Mechanics of Biological Systems* (Vol. 92). Oxford: Oxford University Press.

Bajon, C. H., C.; Motomayor, J.C.; Sauvanet, A.; Robert D. (1999). Megasporogenesis in Arabidopsis thaliana L.: an ultrastructural study. *Sexual Plant Reproduction, 12*(2), 99-109. doi:10.1007/s004970050178

Barbier de Reuille, P., Routier-Kierzkowska, A. L., Kierzkowski, D., Bassel, G. W., Schupbach, T., Tauriello, G., Bajpai, N., Strauss, S., Weber, A., Kiss, A., Burian, A., Hofhuis, H., Sapala, A., Lipowczan, M., Heimlicher, M. B., Robinson, S., Bayer, E. M., Basler, K., Koumoutsakos, P., Roeder, A. H., Aegerter-Wilmsen, T., Nakayama, N., Tsiantis, M., Hay, A., Kwiatkowska, D., Xenarios, I., Kuhlemeier, C., & Smith, R. S. (2015). MorphoGraphX: A platform for quantifying morphogenesis in 4D. *Elife, 4*, 05864. doi:10.7554/eLife.05864

Bassel, G. W., Stamm, P., Mosca, G., Barbier de Reuille, P., Gibbs, D. J., Winter, R., Janka, A., Holdsworth, M. J., & Smith, R. S. (2014). Mechanical constraints imposed by 3D cellular geometry and arrangement modulate growth patterns in the Arabidopsis embryo. *Proc Natl Acad Sci U S A, 111*(23), 8685-8690. doi:10.1073/pnas.1404616111

Beauzamy, L., Nakayama, N., & Boudaoud, A. (2014). Flowers under pressure: ins and outs of turgor regulation in development. *Ann Bot, 114*(7), 1517-1533. doi:10.1093/aob/mcu187

Bencivenga, S., Simonini, S., Benkova, E., & Colombo, L. (2012). The transcription factors BEL1 and SPL are required for cytokinin and auxin signaling during ovule development in Arabidopsis. *Plant Cell, 24*(7), 2886-2897. doi:10.1105/tpc.112.100164

Bichet, A., Desnos, T., Turner, S., Grandjean, O., & Hofte, H. (2001). BOTERO1 is required for normal orientation of cortical microtubules and anisotropic cell expansion in Arabidopsis. *Plant J, 25*(2), 137-148. doi:10.1046/j.1365-313x.2001.00946.x

Boudon, F., Chopard, J., Ali, O., Gilles, B., Hamant, O., Boudaoud, A., Traas, J., & Godin, C. (2015). A computational framework for 3D mechanical modeling of plant morphogenesis with cellular resolution. *PLoS Comput Biol, 11*(1), e1003950. doi:10.1371/journal.pcbi.1003950

Bouquin, T., Mattsson, O., Naested, H., Foster, R., & Mundy, J. (2003). The Arabidopsis lue1 mutant defines a katanin p60 ortholog involved in hormonal control of microtubule orientation during cell growth. *J Cell Sci, 116*(Pt 5), 791-801. doi:10.1242/jcs.00274

Bowman, J. L. e. (Ed.) (1993). *Arabidopsis : an Atlas of Morphology and Development.* Berlin & New York: Springer-Verlag.

Bozorg, B., Krupinski, P., & Jonsson, H. (2016). A continuous growth model for plant tissue. *Phys Biol, 13*(6), 065002. doi:10.1088/1478-3975/13/6/065002

Brodersen, P., Sakvarelidze-Achard, L., Bruun-Rasmussen, M., Dunoyer, P., Yamamoto, Y. Y., Sieburth, L., & Voinnet, O. (2008). Widespread translational inhibition by plant miRNAs and siRNAs. *Science, 320*(5880), 1185-1190. doi:10.1126/science.1159151

Burk, D. H., & Ye, Z. H. (2002). Alteration of oriented deposition of cellulose microfibrils by mutation of a katanin-like microtubule-severing protein. *Plant Cell, 14*(9), 2145-2160. doi:10.1105/tpc.003947

Cao, L., Wang, S., Venglat, P., Zhao, L., Cheng, Y., Ye, S., Qin, Y., Datla, R., Zhou, Y., & Wang, H. (2018). Arabidopsis ICK/KRP cyclin-dependent kinase inhibitors function to ensure the formation of one

megaspore mother cell and one functional megaspore per ovule. *PLoS Genet, 14*(3), e1007230. doi:10.1371/journal.pgen.1007230

Chan, C. J., Heisenberg, C. P., & Hiiragi, T. (2017). Coordination of Morphogenesis and Cell-Fate Specification in Development. *Curr Biol, 27*(18), R1024-R1035. doi:10.1016/j.cub.2017.07.010

Coen, E., Rolland-Lagan, A. G., Matthews, M., Bangham, J. A., & Prusinkiewicz, P. (2004). The genetics of geometry. *Proc Natl Acad Sci U S A, 101*(14), 4728-4735. doi:10.1073/pnas.0306308101

De Storme, N., Keceli, B. N., Zamariola, L., Angenon, G., & Geelen, D. (2016). CENH3-GFP: a visual marker for gametophytic and somatic ploidy determination in Arabidopsis thaliana. *BMC Plant Biol, 16*, 1. doi:10.1186/s12870-015-0700-5

Echevin, E., Le Gloanec, C., Skowronska, N., Routier-Kierzkowska, A. L., Burian, A., & Kierzkowski, D. (2019). Growth and biomechanics of shoot organs. *J Exp Bot, 70*(14), 3573-3585. doi:10.1093/jxb/erz205

Fal, K., Asnacios, A., Chaboute, M. E., & Hamant, O. (2017). Nuclear envelope: a new frontier in plant mechanosensing? *Biophys Rev, 9*(4), 389-403. doi:10.1007/s12551-017-0302-6

Garcia-Aguilar, M., Michaud, C., Leblanc, O., & Grimanelli, D. (2010). Inactivation of a DNA methylation pathway in maize reproductive organs results in apomixis-like phenotypes. *Plant Cell, 22*(10), 3249-3267. doi:10.1105/tpc.109.072181

Godin, C., Gole, C., & Douady, S. (2020). Phyllotaxis as geometric canalization during plant development. *Development, 147*(19). doi:10.1242/dev.165878

Grossniklaus, U., & Schneitz, K. (1998). The molecular and genetic basis of ovule and megagametophyte development. *Semin Cell Dev Biol, 9*(2), 227-238. doi:10.1006/scdb.1997.0214

Gruel, J., Landrein, B., Tarr, P., Schuster, C., Refahi, Y., Sampathkumar, A., Hamant, O., Meyerowitz, E. M., & Jonsson, H. (2016). An epidermis-driven mechanism positions and scales stem cell niches in plants. *Sci Adv, 2*(1), e1500989. doi:10.1126/sciadv.1500989

Hallgrimsson, B., Green, R. M., Katz, D. C., Fish, J. L., Bernier, F. P., Roseman, C. C., Young, N. M., Cheverud, J. M., & Marcucio, R. S. (2019). The developmental-genetics of canalization. *Semin Cell Dev Biol, 88*, 67-79. doi:10.1016/j.semcdb.2018.05.019

Hartmann, J., Wong, M., Gallo, E., & Gilmour, D. (2020). An image-based data-driven analysis of cellular architecture in a developing tissue. *Elife, 9*. doi:10.7554/eLife.55913

Heitzler, P., & Simpson, P. (1991). The choice of cell fate in the epidermis in Drosophila. *Cell, 22*(64(6)), 1083-1092. doi:10.1016/0092-8674(91)90263-x

Hernandez-Lagana, E., & Autran, D. (2020). H3.1 Eviction Marks Female Germline Precursors in Arabidopsis. *Plants (Basel), 9*(10). doi:10.3390/plants9101322

Hervieux, N., Dumond, M., Sapala, A., Routier-Kierzkowska, A. L., Kierzkowski, D., Roeder, A. H., Smith, R. S., Boudaoud, A., & Hamant, O. (2016). A Mechanical Feedback Restricts Sepal Growth and Shape in Arabidopsis. *Curr Biol*. doi:10.1016/j.cub.2016.03.004

Hervieux, N., Tsugawa, S., Fruleux, A., Dumond, M., Routier-Kierzkowska, A. L., Komatsuzaki, T., Boudaoud, A., Larkin, J. C., Smith, R. S., Li, C. B., & Hamant, O. (2017). Mechanical Shielding of Rapidly Growing Cells Buffers Growth Heterogeneity and Contributes to Organ Shape Reproducibility. *Curr Biol, 27*(22), 3468-3479 e3464. doi:10.1016/j.cub.2017.10.033

Huang, A., Rupprecht, J. F., & Saunders, T. E. (2020). Embryonic geometry underlies phenotypic variation in decanalized conditions. *Elife, 9*. doi:10.7554/eLife.47380

Huang, B. Q. R., S.D. (1992). Female Germ Unit: Organization, Isolation, and Function. *International Review of Cytology, 140*, 233-293. doi:10.1016/S0074-7696(08)61099-2

Kawamoto, N., Del Carpio, D. P., Hofmann, A., Mizuta, Y., Kurihara, D., Higashiyama, T., Uchida, N., Torii, K. U., Colombo, L., Groth, G., & Simon, R. (2020). A Peptide Pair Coordinates Regular Ovule Initiation Patterns with Seed Number and Fruit Size. *Curr Biol, 30*(22), 4352-4361 e4354. doi:10.1016/j.cub.2020.08.050

Kennaway, R., Coen, E., Green, A., & Bangham, A. (2011). Generation of diverse biological forms through combinatorial interactions between tissue polarity and growth. *PLoS Comput Biol, 7*(6), e1002071. doi:10.1371/journal.pcbi.1002071

Kimble, J. (2011). Molecular regulation of the mitosis/meiosis decision in multicellular organisms. *Cold Spring Harb Perspect Biol, 3*(8), a002683. doi:10.1101/cshperspect.a002683

Klimyuk, V. I., & Jones, J. D. (1997). AtDMC1, the Arabidopsis homologue of the yeast DMC1 gene: characterization, transposon-induced allelic variation and meiosis-associated expression. *Plant J, 11*(1), 1-14. doi:10.1046/j.1365-313x.1997.11010001.x

Kuchen, E. E., Fox, S., de Reuille, P. B., Kennaway, R., Bensmihen, S., Avondo, J., Calder, G. M., Southam, P., Robinson, S., Bangham, A., & Coen, E. (2012). Generation of leaf shape through early patterns of growth and tissue polarity. *Science, 335*(6072), 1092-1096. doi:10.1126/science.1214678

Landrein, B., Kiss, A., Sassi, M., Chauvet, A., Das, P., Cortizo, M., Laufs, P., Takeda, S., Aida, M., Traas, J., Vernoux, T., Boudaoud, A., & Hamant, O. (2015). Mechanical stress contributes to the expression of the STM homeobox gene in Arabidopsis shoot meristems. *Elife, 4*, e07811. doi:10.7554/eLife.07811

Lempe, J., Lachowiec, J., Sullivan, A. M., & Queitsch, C. (2013). Molecular mechanisms of robustness in plants. *Curr Opin Plant Biol, 16*(1), 62-69. doi:10.1016/j.pbi.2012.12.002

Long, Y., Cheddadi, I., Mosca, G., Mirabet, V., Dumond, M., Kiss, A., Traas, J., Godin, C., & Boudaoud, A. (2020). Cellular Heterogeneity in Pressure and Growth Emerges from Tissue Topology and Geometry. *Curr Biol, 30*(8), 1504-1516 e1508. doi:10.1016/j.cub.2020.02.027

Lora, J., Herrero, M., Tucker, M. R., & Hormaza, J. I. (2017). The transition from somatic to germline identity shows conserved and specialized features during angiosperm evolution. *New Phytol, 216*(2), 495-509. doi:10.1111/nph.14330

Lora, J., Yang, X., & Tucker, M. R. (2019). Establishing a framework for female germline initiation in the plant ovule. *J Exp Bot, 70*(11), 2937-2949. doi:10.1093/jxb/erz212

Luptovciak, I., Komis, G., Takac, T., Ovecka, M., & Samaj, J. (2017). Katanin: A Sword Cutting Microtubules for Cellular, Developmental, and Physiological Purposes. *Front Plant Sci, 8*, 1982. doi:10.3389/fpls.2017.01982

Luptovciak, I., Samakovli, D., Komis, G., & Samaj, J. (2017). KATANIN 1 Is Essential for Embryogenesis and Seed Formation in Arabidopsis. *Front Plant Sci, 8*, 728. doi:10.3389/fpls.2017.00728

Mendes, M. A., Petrella, R., Cucinotta, M., Vignati, E., Gatti, S., Pinto, S. C., Bird, D. C., Gregis, V., Dickinson, H., Tucker, M. R., & Colombo, L. (2020). The RNA dependent DNA methylation pathway is required to restrict SPOROCYTELESS/NOZZLE expression to specify a single female germ cell precursor in Arabidopsis. *Development*. doi:10.1242/dev.194274

Mendocilla-Sato, E. B., C. (2017). Analysis of 3D Cellular Organization of Fixed Plant Tissues Using a User-guided Platform for Image Segmentation. *Bio-protocols, 7*(12), e2355. doi:10.21769/BioProtoc.2355

Mosca, G. A., M.; Strauss, S.; Runions, R.; Sapala, A.; Smith, R.S. (2018). Modeling plant tissue growth and cell division *Mathematical Modelling in Plant Biology* (pp. 107-138): Springer, Cham.

Nonomura, K., Miyoshi, K., Eiguchi, M., Suzuki, T., Miyao, A., Hirochika, H., & Kurata, N. (2003). The MSP1 gene is necessary to restrict the number of cells entering into male and female sporogenesis and to initiate anther wall formation in rice. *Plant Cell, 15*(8), 1728-1739. doi:10.1105/tpc.012401

Olmedo-Monfil, V., Duran-Figueroa, N., Arteaga-Vazquez, M., Demesa-Arevalo, E., Autran, D., Grimanelli, D., Slotkin, R. K., Martienssen, R. A., & Vielle-Calzada, J. P. (2010). Control of female gamete formation by a small RNA pathway in Arabidopsis. *Nature, 464*(7288), 628-632. doi:10.1038/nature08828

Ovecka, M., Luptovciak, I., Komis, G., Samajova, O., Samakovli, D., & Samaj, J. (2020). Spatiotemporal Pattern of Ectopic Cell Divisions Contribute to Mis-Shaped Phenotype of Primary and Lateral Roots of katanin1 Mutant. *Front Plant Sci, 11*, 734. doi:10.3389/fpls.2020.00734

Peaucelle, A., Braybrook, S. A., Le Guillou, L., Bron, E., Kuhlemeier, C., & Hofte, H. (2011). Pectin-induced changes in cell wall mechanics underlie organ initiation in Arabidopsis. *Curr Biol, 21*(20), 1720-1726. doi:10.1016/j.cub.2011.08.057

Pinto, S. C., Mendes, M. A., Coimbra, S., & Tucker, M. R. (2019). Revisiting the Female Germline and Its Expanding Toolbox. *Trends Plant Sci, 24*(5), 455-467. doi:10.1016/j.tplants.2019.02.003

Pujadas, E., & Feinberg, A. P. (2012). Regulated noise in the epigenetic landscape of development and disease. *Cell, 148*(6), 1123-1131. doi:10.1016/j.cell.2012.02.045

Reik, W., & Surani, M. A. (2015). Germline and Pluripotent Stem Cells. *Cold Spring Harb Perspect Biol, 7*(11). doi:10.1101/cshperspect.a019422

Ren, H., Dang, X., Cai, X., Yu, P., Li, Y., Zhang, S., Liu, M., Chen, B., & Lin, D. (2017). Spatio-temporal orientation of microtubules controls conical cell shape in Arabidopsis thaliana petals. *PLoS Genet, 13*(6), e1006851. doi:10.1371/journal.pgen.1006851

Rodriguez-Leal, D., Leon-Martinez, G., Abad-Vivero, U., & Vielle-Calzada, J. P. (2015). Natural variation in epigenetic pathways affects the specification of female gamete precursors in Arabidopsis. *Plant Cell, 27*(4), 1034-1045. doi:10.1105/tpc.114.133009

Rodriguez, E. K., Hoger, A., & McCulloch, A. D. (1994). Stress-dependent finite growth in soft elastic tissues. *J Biomech, 27*(4), 455-467. doi:10.1016/0021-9290(94)90021-3

Royer, C., Leonavicius, K., Kip, A., Fortin, D., Nandi, K., Vincent, A., Jones, C., Child, T., Coward, K., Graham, C., & Srinivas, S. (2020). Establishment of a relationship between blastomere geometry and YAP localisation during compaction. *Development, 147*(19). doi:10.1242/dev.189449

Savaldi-Goldstein, S., Peto, C., & Chory, J. (2007). The epidermis both drives and restricts plant shoot growth. *Nature, 446*(7132), 199-202. doi:10.1038/nature05618

Scharloo. (1991). Canalization: Genetic and Developmental Aspects. *Annual Review of Ecology and Systematics, 22*, 65-93. doi:10.1146/annurev.es.22.110191.000433

Schmidt, A., Schmid, M. W., & Grossniklaus, U. (2015). Plant germline formation: common concepts and developmental flexibility in sexual and asexual reproduction. *Development, 142*(2), 229-241. doi:10.1242/dev.102103

Schmidt, A., Wuest, S. E., Vijverberg, K., Baroux, C., Kleen, D., & Grossniklaus, U. (2011). Transcriptome analysis of the Arabidopsis megaspore mother cell uncovers the importance of RNA helicases for plant germline development. *PLoS Biol, 9*(9), e1001155. doi:10.1371/journal.pbio.1001155

Schneitz, K. H. M. P. R. E. (1995). Wild-type ovule development in Arabidopsis thaliana: a light microscope study of cleared whole-mount tissue. *Plant Journal, 7*(5), 731-749. doi:10.1046/j.1365-313X.1995.07050731.x

She, W., Grimanelli, D., Rutowicz, K., Whitehead, M. W., Puzio, M., Kotlinski, M., Jerzmanowski, A., & Baroux, C. (2013). Chromatin reprogramming during the somatic-to-reproductive cell fate transition in plants. *Development, 140*(19), 4008-4019. doi:10.1242/dev.095034

Sheridan, W. F., Avalkina, N. A., Shamrov, II, Batygina, T. B., & Golubovskaya, I. N. (1996). The mac1 gene: controlling the commitment to the meiotic pathway in maize. *Genetics, 142*(3), 1009-1020.

Sheridan, W. F., Golubeva, E. A., Abrhamova, L. I., & Golubovskaya, I. N. (1999). The mac1 mutation alters the developmental fate of the hypodermal cells and their cellular progeny in the maize anther. *Genetics, 153*(2), 933-941.

Smith, R. S. (2009). Modeling plant morphogenesis and growth. . In M. G. Ben Amar, A.; Müller, M.M.; Cugliandolo, L. (Ed.), *New Trends in the Physics andMechanics of Biological Systems. Lecture Notes of the Les Houches Summer School.* (Vol. 22). Oxford: Oxford University Press.

Strzalka, W., & Ziemienowicz, A. (2011). Proliferating cell nuclear antigen (PCNA): a key factor in DNA replication and cell cycle regulation. *Ann Bot, 107*(7), 1127-1140. doi:10.1093/aob/mcq243

Su, Z., Wang, N., Hou, Z., Li, B., Li, D., Liu, Y., Cai, H., Qin, Y., & Chen, X. (2020). Regulation of Female Germline Specification via Small RNA Mobility in Arabidopsis. *Plant Cell, 32*(9), 2842-2854. doi:10.1105/tpc.20.00126

Su, Z., Zhao, L., Zhao, Y., Li, S., Won, S., Cai, H., Wang, L., Li, Z., Chen, P., Qin, Y., & Chen, X. (2017). The THO Complex Non-Cell-Autonomously Represses Female Germline Specification through the TAS3-ARF3 Module. *Curr Biol, 27*(11), 1597-1609 e1592. doi:10.1016/j.cub.2017.05.021

Truernit, E., Bauby, H., Dubreucq, B., Grandjean, O., Runions, J., Barthelemy, J., & Palauqui, J. C. (2008). High-resolution whole-mount imaging of three-dimensional tissue organization and gene expression enables the study of Phloem development and structure in Arabidopsis. *Plant Cell, 20*(6), 1494-1503. doi:10.1105/tpc.107.056069

Tucker, M. R., Okada, T., Hu, Y., Scholefield, A., Taylor, J. M., & Koltunow, A. M. (2012). Somatic small RNA pathways promote the mitotic events of megagametogenesis during female reproductive development in Arabidopsis. *Development, 139*(8), 1399-1404. doi:10.1242/dev.075390

Ubeda-Tomas, S., Federici, F., Casimiro, I., Beemster, G. T., Bhalerao, R., Swarup, R., Doerner, P., Haseloff, J., & Bennett, M. J. (2009). Gibberellin signaling in the endodermis controls Arabidopsis root meristem size. *Curr Biol, 19*(14), 1194-1199. doi:10.1016/j.cub.2009.06.023

Uyttewaal, M., Burian, A., Alim, K., Landrein, B., Borowska-Wykret, D., Dedieu, A., Peaucelle, A., Ludynia, M., Traas, J., Boudaoud, A., Kwiatkowska, D., & Hamant, O. (2012). Mechanical stress acts via katanin to amplify differences in growth rate between adjacent cells in Arabidopsis. *Cell, 149*(2), 439-451. doi:10.1016/j.cell.2012.02.048

Vijayan, A., Tofanelli, R., Strauss, S., Cerrone, L., Wolny, A., Strohmeier, J., Kreshuk, A., Hamprecht, F. A., Smith, R. S., & Schneitz, K. (2020). A digital 3D reference atlas reveals cellular growth patterns shaping the Arabidopsis ovule. *bioRxiv*, 2020.2009.2019.303560. doi:10.1101/2020.09.19.303560

Waddington, C. H. (1942). Canalization of development and the inheritance of acquired characters. *Nature*(150), 563-565.

Whitewoods, C. D., & Coen, E. (2017). Growth and Development of Three-Dimensional Plant Form. *Curr Biol, 27*(17), R910-R918. doi:10.1016/j.cub.2017.05.079

Wightman, R., Chomicki, G., Kumar, M., Carr, P., & Turner, S. R. (2013). SPIRAL2 determines plant microtubule organization by modulating microtubule severing. *Curr Biol, 23*(19), 1902-1907. doi:10.1016/j.cub.2013.07.061

Wolny, A., Cerrone, L., Vijayan, A., Tofanelli, R., Barro, A. V., Louveaux, M., Wenzl, C., Strauss, S., Wilson-Sanchez, D., Lymbouridou, R., Steigleder, S., Pape, C., Bailoni, A., Duran-Nebreda, S., Bassel, G., Lohmann, J. U., Tsiantis, M., Hamprecht, F., Schneitz, K., Maizel, A., & Kreshuk, A. (2020). Accurate and versatile 3D segmentation of plant tissues at cellular resolution. *Elife, 9*. doi:10.7554/eLife.57613

Yokoyama, R., Hirakawa, T., Hayashi, S., Sakamoto, T., & Matsunaga, S. (2016). Dynamics of plant DNA replication based on PCNA visualization. *Sci Rep, 6*, 29657. doi:10.1038/srep29657

Zhang, Q., Fishel, E., Bertroche, T., & Dixit, R. (2013). Microtubule severing at crossover sites by katanin generates ordered cortical microtubule arrays in Arabidopsis. *Curr Biol, 23*(21), 2191-2195. doi:10.1016/j.cub.2013.09.018

Zhao, X., Bramsiepe, J., Van Durme, M., Komaki, S., Prusicki, M. A., Maruyama, D., Forner, J., Medzihradszky, A., Wijnker, E., Harashima, H., Lu, Y., Schmidt, A., Guthorl, D., Logrono, R. S., Guan, Y., Pochon, G., Grossniklaus, U., Laux, T., Higashiyama, T., Lohmann, J. U., Nowack, M. K., & Schnittger, A. (2017). RETINOBLASTOMA RELATED1 mediates germline entry in Arabidopsis. *Science, 356*(6336). doi:10.1126/science.aaf6532

Zhao, X., de Palma, J., Oane, R., Gamuyao, R., Luo, M., Chaudhury, A., Herve, P., Xue, Q., & Bennett, J. (2008). OsTDL1A binds to the LRR domain of rice receptor kinase MSP1, and is required to limit sporocyte numbers. *Plant J, 54*(3), 375-387. doi:10.1111/j.1365-313X.2008.03426.x

1151